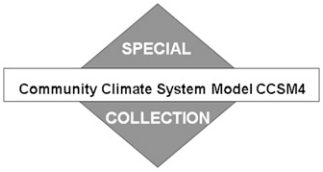

The CCSM4 Ocean Component

GOKHAN DANABASOGLU, SUSAN C. BATES, AND BRUCE P. BRIEGLEB

National Center for Atmospheric Research, Boulder, Colorado

STEVEN R. JAYNE

Woods Hole Oceanographic Institution, Woods Hole, Massachusetts

MARKUS JOCHUM, WILLIAM G. LARGE, SYNTE PEACOCK, AND STEVE G. YEAGER

National Center for Atmospheric Research, Boulder, Colorado

(Manuscript received 9 February 2011, in final form 3 August 2011)

ABSTRACT

The ocean component of the Community Climate System Model version 4 (CCSM4) is described, and its solutions from the twentieth-century (20C) simulations are documented in comparison with observations and those of CCSM3. The improvements to the ocean model physical processes include new parameterizations to represent previously missing physics and modifications of existing parameterizations to incorporate recent new developments. In comparison with CCSM3, the new solutions show some significant improvements that can be attributed to these model changes. These include a better equatorial current structure, a sharper thermocline, and elimination of the cold bias of the equatorial cold tongue all in the Pacific Ocean; reduced sea surface temperature (SST) and salinity biases along the North Atlantic Current path; and much smaller potential temperature and salinity biases in the near-surface Pacific Ocean. Other improvements include a global-mean SST that is more consistent with the present-day observations due to a different spinup procedure from that used in CCSM3. Despite these improvements, many of the biases present in CCSM3 still exist in CCSM4. A major concern continues to be the substantial heat content loss in the ocean during the preindustrial control simulation from which the 20C cases start. This heat loss largely reflects the top of the atmospheric model heat loss rate in the coupled system, and it essentially determines the abyssal ocean potential temperature biases in the 20C simulations. There is also a deep salty bias in all basins. As a result of this latter bias in the deep North Atlantic, the parameterized overflow waters cannot penetrate much deeper than in CCSM3.

1. Introduction

The Community Climate System Model version 4 (CCSM4) was released to the community in April 2010. A general description of the CCSM4 and some of the major improvements in its solutions in comparison with its previous version CCSM3 are presented in Gent et al. (2011). The primary purposes of this paper are i) to describe the CCSM4 ocean component, highlighting major developments since CCSM3; ii) to document the CCSM4 ocean model solutions from the twentieth-century (20C) simulations in comparison with available observations and those of CCSM3, presenting improvements as well as existing biases in CCSM4; and iii) to assess the consequences of two different spinup procedures used in CCSM3 and CCSM4 on the deep ocean properties. In addition, the solutions from an ocean–sea ice hindcast case forced with interannually varying atmospheric data are documented in comparison with observations as well as the 20C simulations, the former to assess the fidelity of the forced ocean simulations and the latter for possible attribution of ocean model biases in the coupled integrations. Here, we focus on the nominal 1° horizontal resolution version of the ocean model. The CCSM4 coupled solutions are from the version that also uses nominal 1° horizontal resolution in its atmospheric component. The description of the nominal 3° horizontal resolution ocean model and the results from

Corresponding author address: G. Danabasoglu, National Center for Atmospheric Research, P. O. Box 3000, Boulder, CO 80307. E-mail: gokhan@ucar.edu

DOI: 10.1175/JCLI-D-11-00091.1

CCSM4 simulations that use this coarser-resolution ocean coupled to a T31 atmospheric model are discussed in Shields et al. (2012).

The ocean component of the CCSM4 is a level-coordinate model based on the Parallel Ocean Program (POP) of the Los Alamos National Laboratory (Smith et al. 2010). The present version differs significantly from the one described in Danabasoglu et al. (2006) used in the CCSM3 simulations; the base code has been updated to POP version 2 (POP2) and many physical and numerical software developments have been incorporated. A significant fraction of the new subgrid-scale parameterizations were realized through our collaborations with the university communities that participated in the U.S. Climate Variability and Predictability (CLIVAR) Climate Process Team (CPT) activities. Specifically, the CPTs on gravity current entrainment and eddy–mixed layer interactions resulted in an overflow parameterization (Danabasoglu et al. 2010), a near-surface eddy flux parameterization (Danabasoglu et al. 2008), a prescription for lateral tracer diffusivities that vary in the vertical (Danabasoglu and Marshall 2007), and a submesoscale mixed layer eddy parameterization (Fox-Kemper et al. 2011). Other major changes since CCSM3 include increased vertical resolution in the upper ocean, incorporation of an abyssal tidal mixing parameterization (Jayne 2009), and new prescriptions for anisotropic horizontal viscosities (Jochum et al. 2008) as well as background vertical diffusivities and viscosities (Jochum 2009).

As listed above, another aspect considered in this study is the impact of different spinup procedures used in CCSM3 and CCSM4 to obtain initial conditions for the 20C simulations (Gent et al. 2011). The CCSM3 strategy was to obtain a relatively well-balanced top of the atmosphere model (TOA) heat flux in the present-day control integration. The 1870 preindustrial control used the same tuning. The 20C ensemble members subsequently started from various stages of this 1870 control. In contrast, with the CCSM4 simulations, the objective was to get a well-balanced TOA heat flux in the 1850 preindustrial control. The 20C cases were then started from various points in this control. In CCSM coupled simulations, any TOA heat flux imbalances are largely reflected as corresponding heat content changes in the ocean component, particularly at depth. Therefore, differing TOA heat flux imbalances and differing lengths of the preindustrial controls prior to the start of the 20C simulations in CCSM3 and CCSM4 dictate the abyssal ocean biases in the subsequent 20C cases. This is because these order 150-yr experiments are too short to produce any significant departures at depth from their initial conditions.

In this work, we present mostly time-mean results. Other aspects of the ocean model solutions from CCSM4 simulations are discussed in several *Journal of Climate* CCSM4 Special Issue papers. These include papers on multidecadal variability in the North Atlantic with a focus on the Atlantic meridional overturning circulation (AMOC) (Danabasoglu et al. 2011, manuscript submitted to *J. Climate*), mean biases, variability, and trends in air–sea fluxes and upper ocean (Bates et al. 2011, manuscript submitted to *J. Climate*), Southern Ocean (Weijer et al. 2012), tropical Atlantic Ocean variability and biases (Munoz et al. 2011, manuscript submitted to *J. Climate*; Grodsky et al. 2012) and oceanic changes in the twenty-first century (S. Peacock et al. 2011, unpublished manuscript). The paper is organized as follows. The ocean model setup and details of the parameterizations along with the experiments used are given in section 2. The results are presented in section 3. Section 4 presents a summary and conclusions.

2. Ocean model

POP2 solves the primitive equations in general orthogonal coordinates in the horizontal with the hydrostatic and Boussinesq approximations. A linearized, implicit free-surface formulation is used for the barotropic equation. This formulation allows variations of the surface layer thickness, Δz_1. However, because of the linearization assumption, Δz_1 cannot be very thin and has to be larger than order a few meters. The global integral of the ocean volume remains constant because the freshwater fluxes are treated as virtual salt fluxes, using a constant reference salinity. Below, we present a summary of the ocean model setup and major developments since CCSM3.

The standard ocean model uses the same horizontal grid with its displaced grid North Pole and nominal 1° resolution described in Danabasoglu et al. (2006). However, the number of vertical levels has been increased from 40 levels in CCSM3 to 60 levels in the present version. Most of this increase occurs in the upper ocean where the resolution is uniform at 10 m in the upper 160 m. The vertical grid spacing increases to 250 m by a depth of about 3500 m, below which it remains constant. Because of the change in model vertical resolution, the discrete bottom topography was recreated using a smooth (one pass of a 9-point Gaussian filter) version of the 2-min gridded global relief data (National Geophysical Data Center 2006). The minimum and maximum ocean depths were set to 30 and 5500 m, respectively, and isolated holes were eliminated. To improve transports through some straits and passages, the discrete topography and land–ocean mask were modified, particularly in the Indonesian Throughflow (ITF) region. Additional changes were then incorporated in the overflow regions as discussed below.

Along with the ITF, the inclusions of the Galapagos and Kuril Islands and opening of the Nares Strait, linking the Baffin Bay with the Arctic Ocean, are the only main differences in the land–ocean masks between CCSM4 and that of CCSM3.

A new overflow parameterization of density driven flows (OFP; Danabasoglu et al. 2010; Briegleb et al. 2010) is used to represent the Denmark Strait (DS), Faroe Bank Channel (FBC), Ross Sea (RS), and Weddell Sea (WS) overflows. The OFP represents exchanges through narrow straits and channels, associated entrainment, and subsequent injection of overflow product waters into the abyssal basins. These processes with horizontal and vertical length scales as small as 1 km and 10 m, respectively, require much finer horizontal and vertical resolutions than typically used in ocean models for climate studies, making their explicit representation prohibitively expensive. The OFP also addresses the chronic, shallow penetration depth bias of deep waters in level coordinate models as POP2. The parameterization is based on the Marginal Sea Boundary Condition (MSBC) scheme of Price and Yang (1998). However, there are significant differences between the MSBC and the OFP. To accommodate the numerical requirements of the OFP, such as having three or more sidewall grid points at the same depth levels as the source, entrainment, and product sites and the need to widen some downstream choke points to allow deep product water easier access to abyssal basins, we have modified the bottom topography. For example, the entire region from the Iceland–Scotland ridge to the actual geographic FBC was widened and flattened. Further details of the bottom topography changes and of the OFP are given in Danabasoglu et al. (2010) and Briegleb et al. (2010). For simplicity, a cliff topography is used to the immediate west of the sill at the Gibraltar Strait for the Mediterranean overflow instead of the OFP (Wu et al. 2007). The cliff depth exceeds 1450 m, deeper than the observed depth range of the Mediterranean Overflow Water. Such a configuration avoids excessive entrainment associated with a staircase topography and lets the level of neutral buoyancy develop through the usual level coordinate vertical mixing. The same approach was also used in CCSM3 but with a less cliff-like topography.

The model tracer equations use the Gent and McWilliams (1990, hereafter referred to as GM90) isopycnal transport parameterization in its skew-flux form (Griffies 1998). This parameterization was developed for the quasi-adiabatic ocean interior and is not valid near the boundaries. A practice has been to taper the effects of parameterized eddy fluxes as the boundaries are approached. This approach is not physical, particularly near the surface where diabatic mesoscale fluxes may dominate mixing. We include the effects of these diabatic mesoscale fluxes within the surface diabatic layer, using a simplified version of the near-boundary eddy flux parameterization of Ferrari et al. (2008), as implemented by Danabasoglu et al. (2008). Within this layer, the eddy-induced (bolus) velocity does not vanish. It is set parallel to the surface and has no vertical shear. The need for any ad-hoc, near-surface taper functions is eliminated. In the ocean interior, the diffusivity coefficients are tapered for isopycnal slopes greater than 0.3. Both the thickness and isopycnal diffusivity coefficients used in GM90 vary identically in the vertical, following Ferreira et al. (2005) and Danabasoglu and Marshall (2007). In the upper ocean, we use enhanced diffusivity values that can be as large as 3000 $m^2\ s^{-1}$. They diminish to 300 $m^2\ s^{-1}$ by a depth of about 2000 m. In the surface diabatic layer, the horizontal diffusivity coefficient is set also to 3000 $m^2\ s^{-1}$. The restratification effects of the finite-amplitude, submesoscale mixed layer eddies are included, using the mixed layer eddy parameterization of Fox-Kemper et al. (2008) as implemented by Fox-Kemper et al. (2011). The parameterization is cast in terms of an overturning streamfunction. We use 5000 m as the minimum local width of the mixed layer fronts; 1 day as the momentum mixing time scale across the mixed layer; and 0.07 as the efficiency coefficient.

As in CCSM3, we use the Large et al. (2001) anisotropic horizontal viscosity formulation in its generalized form (Smith and McWilliams 2003) in the momentum equations with the viscosity coefficients differing arbitrarily in the east–west and north–south directions. However, unlike in CCSM3, these coefficients no longer depend on either the local deformation rate or the grid Reynolds number. Instead of the latter, elevated viscosities at the western boundaries are used in both directions. This follows the Munk (1950) criterion, resolving the viscous western boundary currents as well as diminishing numerical noise. The minimum east–west viscosity is 600 $m^2\ s^{-1}$. In the north–south direction, the minimum viscosity increases from an equatorial value of 600 to 1200 $m^2\ s^{-1}$ by 45° of latitude. The resulting viscosities are time independent. With a 1-h time step, the values for both coefficients remain below what is allowed by the diffusive stability criterion at all latitudes. In addition, the viscosities are generally much smaller than the ones used in CCSM3, particularly at low latitudes and in the vicinity of western boundary currents. For example, at the equator, CCSM4 uses 600 $m^2\ s^{-1}$ for both viscosity components, smaller than 1000 $m^2\ s^{-1}$ for the north–south viscosity and considerably smaller than $>60\,000\ m^2\ s^{-1}$ for the east–west viscosity employed in CCSM3. Further details of this new prescription are given in Jochum et al. (2008).

The background internal wave mixing diffusivity used in the *K*-Profile Parameterization (KPP) vertical mixing

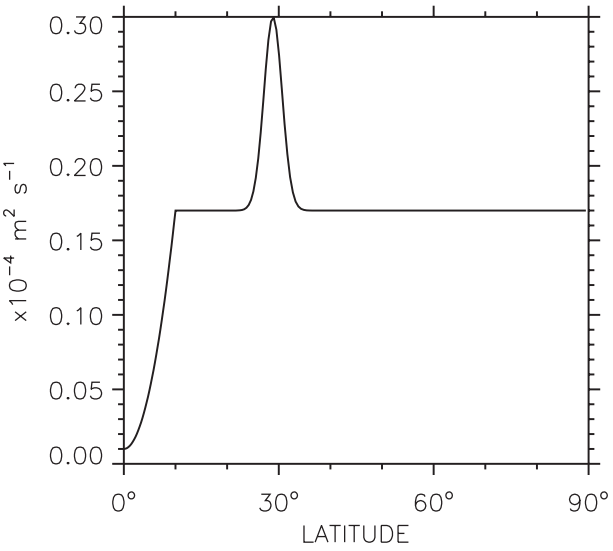

FIG. 1. Background internal wave mixing vertical diffusivity. The latitudinal variation is symmetric about the equator.

parameterization (Large et al. (1994) as modified by Danabasoglu et al. (2006)) has a latitudinal structure based on observational and theoretical evidence as discussed in Jochum (2009). The minimum and maximum background diffusivities are 0.01×10^{-4} and 0.30×10^{-4} m^2 s^{-1}, occurring at the equator and at about 30° of latitude, respectively (Fig. 1). Elsewhere, a value of 0.17×10^{-4} m^2 s^{-1} is used and the distribution is symmetric about the equator. In addition, following Jochum and Potemra (2008), the background diffusivity is enhanced to 1×10^{-4} m^2 s^{-1} only in the Banda Sea region (near the ITF). Unlike in CCSM3, these diffusivities do not vary in the vertical. Instead, the abyssal tidal mixing parameterization of St.Laurent et al. (2002) as implemented by Jayne (2009)—with a fixed energy flux—is used to represent the deep vertical mixing arising from the breaking of tidally generated internal waves over rough topography. The maximum diffusivity due to tidal mixing is set to 100×10^{-4} m^2 s^{-1}. Also, we use 0.33 as the fraction of the total internal wave energy flux available for local dissipation; 0.2 as the turbulence mixing efficiency; and 500 m as the *e*-folding length scale. In addition, to partially alleviate tracer extremes mostly associated with advective dispersion errors at depth, we do not allow decreasing tidal diffusivities with depth over the deepest two levels of model bottom topography. As in CCSM3, the turbulent Prandtl number is 10. In regions of interior static instability, the diffusivity and viscosity coefficients are increased to 1 m^2 s^{-1}.

The diurnal cycle of the daily, net shortwave heat flux depends on the solar zenith angle, which is determined from longitude, latitude, time of year, and the solar declination angle. As in CCSM3, a river transport model (Oleson et al. 2010) routes runoff from the land surface to the ocean model via the flux coupler. These runoff fluxes are treated as surface freshwater fluxes, and they are distributed over coastal ocean points near the river mouths, with higher concentrations at the mouths. However, because the land model does not account for the heat flux associated with snow and ice melt to liquid runoff, this accounting is done within the ocean model to conserve heat in the coupled system. Therefore, when the land model is prognostic, the ocean model receives an ice runoff field in addition to the liquid runoff. The ocean model then loses heat to account for the phase change from ice to liquid runoff. The total freshwater flux due to runoff is the sum of liquid and ice runoffs. The other aspects of the CCSM4 ocean model setup—such as once-a-day coupling frequency, a third-order upwind advection scheme for tracers, a second-order central advection scheme for momentum, and treatment of marginal sea freshwater fluxes in coupled simulations—remain the same as in CCSM3 (see Danabasoglu et al. 2006).

Experiments

For the CCSM4 analysis presented herein, we use the 1850 preindustrial control integration (1850 CONTROL) and five members of the 20C ensemble simulations described in Gent et al. (2011). Prior to 1850 CONTROL, a preliminary preindustrial simulation was integrated for 130 yr, starting with the January-mean climatological Polar Science Center Hydrographic Climatology (PHC2) potential temperature (θ) and salinity (S) data [PHC2 dataset represents a blending of the Levitus et al. (1998) and Steele et al. (2001) data for the Arctic Ocean] and state of rest in the ocean model. After updating to new datasets (e.g., ozone) and retuning, the primary 1850 CONTROL was started from the end of the preliminary simulation. The 1850 CONTROL was integrated for 1300 yr. The 20C cases were integrated for 156 yr each from January 1850 to December 2005, starting from 1 January of yr 863, 893, 937, 983, and 1031 of 1850 CONTROL. These start dates were chosen to sample different phases of the AMOC variability (see G. Danabasoglu et al. 2011, unpublished manuscript).

The CCSM3 1870 preindustrial control case was integrated for 950 yr with several changes during the course of the integration (Bryan et al. 2006; Gent et al. 2006). It started from present-day θ and S distributions and zero velocity. The eight 20C ensemble integrations were initialized from this preindustrial control between yr 360 and 540, starting from 1 January. Each member was run for 130 yr from January 1870 to December 1999.

Both CCSM3 and CCSM4 preindustrial simulations are utilized to document the ocean model drift and sources of abyssal biases in the respective 20C simulations. We use the 20C simulations to compare ocean model solutions to available *present-day* observations. For CCSM4, the observational comparisons are based on the five-member ensemble mean for the 1986–2005 mean. For CCSM3, we use ensemble mean fields for the 1980–99 mean. To the extent possible, we make use of all eight CCSM3 ensemble members, but not all the fields are available from all members, for example, only three members carry chlorofluorocarbons. We refer to these CCSM4 and CCSM3 ensemble- and time-mean solutions as CCSM4 and CCSM3, respectively.

The ocean–sea ice coupled hindcast integration (OCN) is forced with the Coordinated Ocean-Ice Reference Experiments (CORE; Griffies et al. 2009) interannually varying atmospheric datasets for the 60-yr cycle for 1948–2007 (Large and Yeager 2009). In OCN, a weak salinity restoring to the monthly-mean PHC2 dataset is applied. This restoring uses a 4-yr time scale over 50 m, and its global mean is subtracted every model time step. Thus, the restoring flux does not contribute to the global salt budget. For OCN, we use the 20-yr mean corresponding to yr 1986–2005 (as in CCSM4) from the fourth forcing cycle in our analysis.

3. Model solutions

a. Model drift and deep θ and S

By the end of the 1300-yr CCSM4 1850 CONTROL simulation, the global volume-mean potential temperature $\langle\theta\rangle$ is down to 3.13°C in the ocean model, representing a cooling of 0.42°C from the initial conditions. This cooling largely reflects the TOA heat loss in the coupled system. The oceanic heat loss rate remains rather steady at -0.14 W m^{-2} ($=-0.10$ W m^{-2} when scaled by the entire surface area of the earth, corresponding to $\frac{2}{3}$ of the TOA heat loss rate of -0.15 W m^{-2}) over the last 700 yr. This is only slightly lower than the heat loss rate of -0.17 W m^{-2} seen during the first 600 yr. Thus, the initial global $\langle\theta\rangle$ in the 20C simulations range from 3.26°C for the first ensemble member starting at yr 863 to 3.21°C for the last member starting at yr 1031 of the 1850 CONTROL.

In contrast, the oceanic heat loss rate is much larger in the CCSM3 preindustrial control simulation, remaining steady at about -0.65 W m^{-2} after about yr 200. Fortunately, compared to the CCSM4 strategy, the 20C simulations in CCSM3 were started much earlier from the preindustrial control. Therefore, the initial global $\langle\theta\rangle$ is 3.25°C in the first 20C case starting at yr 360 and 3.01°C in the last member starting at yr 560 of the preindustrial control. However, seven of the 20C ensemble members were initialized before yr 460 at which time the global $\langle\theta\rangle$ was 3.12°C. Thus, in both CCSM3 and CCSM4, the 20C simulations start with rather comparable global $\langle\theta\rangle$ despite their quite different spin-up procedures.

We show the time series of the vertical profiles of the horizontal-mean θ from 1850 CONTROL in comparison with the PHC2 dataset in Fig. 2. This represents a comparison of our 1850 CONTROL simulation to present-day observations. In addition to the global ocean evolution, Pacific, Indian, and Atlantic Ocean time series are included in the figure. Here, the southern boundaries of the basins extend to 34°S; the Atlantic basin excludes all the peripheral marginal seas and the Arctic Ocean, and the ITF region south of 3°S and the region between Australia and New Guinea are included in the Indian basin.

The global time series show that the ocean continuously loses heat at all depths, and it is colder than observations throughout the water column by the end of the simulation (Fig. 2a). In particular, the largest cold biases in excess of $-0.5°$ and -0.6°C occur between 250- and 375-m depth and between 1600- and 2500-m depth, respectively. All the other major ocean basins, taken individually, also lose heat throughout the integration at all depths. The largest cold bias is in excess of -1.5°C, occurring at about 1000-m depth in the Indian Ocean. Some depth ranges, however, still remain warmer than observations after 1300 yr, for example, between the 25- and 425-m-depth range in the Indian Ocean and below about 500-m depth in the Atlantic Ocean.

The global volume-mean S diminishes from its initial value of 34.7219 to 34.7184 psu by the end of 1850 CONTROL. Most of this reduction occurs during the first 850 yr—at an overall rate of -3.7×10^{-4} psu century^{-1}—prior to the aquifer water correction in the land model (Gent et al. 2011). After this correction, the trend is reduced by an order of magnitude to -4.6×10^{-5} psu century^{-1}. This trend is about 25% smaller than in the CCSM3 present-day control simulation (Collins et al. 2006), but it is comparable to the trend in the CCSM3 preindustrial control for yr 325–650 during which the 20C simulations started. Despite the relatively small global-mean trend, S gets redistributed within the ocean, showing different trends with depth (Fig. 3). While the upper ocean freshens by as much as 0.4 psu, the deep ocean below 1500-m depth is saltier than PHC2 data by >0.1 psu. The corresponding time series for the Atlantic, Pacific, and Indian Oceans (not shown) are broadly similar to Fig. 3, with upper-ocean freshening and deep salinification. However, bias magnitudes and demarcation

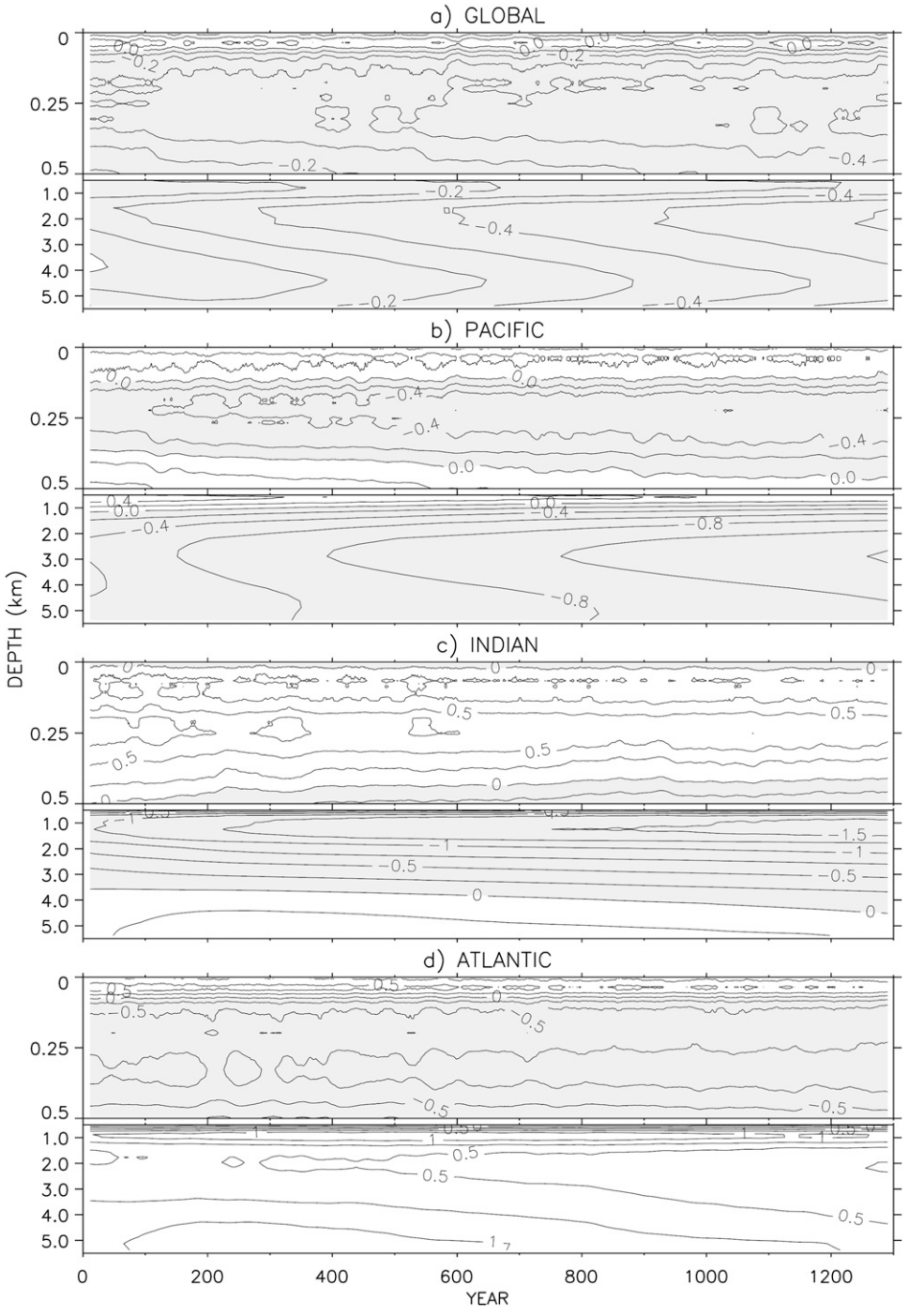

FIG. 2. Horizontal-mean potential temperature difference time series for 1850 CONTROL minus PHC2 observations: (a) global, (b) Pacific, (c) Indian, and (d) Atlantic Oceans. The contour intervals are 0.1°, 0.2°, 0.25°, and 0.25°C in (a),(b),(c),(d), respectively. The shaded regions indicate negative differences. The time series are based on annual-mean fields smoothed using a 10-yr running mean.

depths differ among basins. For example, while the Atlantic Ocean gets saltier below 500-m depth by >0.25 psu, the Pacific and Indian basins get saltier below 2000-m depth by >0.05 psu and >0.15 psu, respectively, by yr 1300. The fresh bias exceeds 1 psu in the upper-ocean Indian basin.

We show the zonal-mean θ and S CCSM4 minus PHC2 climatology difference distributions in Fig. 4. The

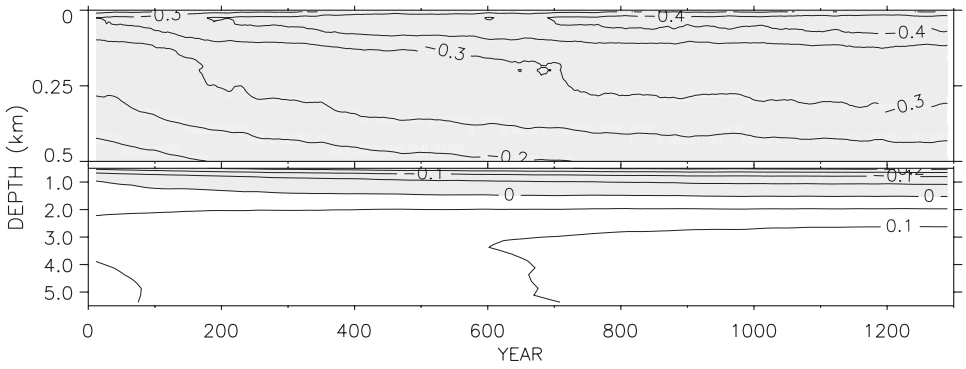

FIG. 3. Horizontal-mean salinity difference time series for 1850 CONTROL minus PHC2 observations for the global oceans. The contour interval is 0.05 psu. The shaded regions indicate negative differences. The time series are based on annual-mean fields smoothed using a 10-yr running mean.

20C deep ocean biases reflect the biases that exist in 1850 CONTROL between yr 863 and 1031 as each ensemble member was initialized from 1850 CONTROL during this period. Because the 20C simulations are run only for 156 yr, the deep ocean does not deviate noticeably from its initial states. The figure shows that the deep Pacific Ocean is broadly colder than the PHC2 climatology by >1°C. The deep cold bias in the Indian Ocean peaks at about −3°C at 1000-m depth at the northern edge of the basin. There is a corresponding fresh bias of >0.6 psu (Fig. 4f). These biases are likely due to the unresolved and unparameterized Persian Gulf and, particularly, Red Sea overflows. The deep Atlantic Ocean remains generally warmer than observed by about 0.5°C in the mean. The local θ and S maxima between 20° and 30°N at a depth of about 1000 m (Figs. 4g,h) are associated with the warmer and saltier than observed Mediterranean outflow through the Strait of Gibraltar. The θ biases in the upper 500 m reach several °C in magnitude, but they are not uniform across basins. For example, the Indian Ocean is warmer than observed with a maximum bias of >3°C at its northern boundary, whereas there are cold biases of >2°C in the South Pacific as well as south of 20°N in the Atlantic basin below about 100 m depth.

Consistent with Fig. 3, the zonal-mean CCSM4 minus PHC2 S differences reveal generally fresher waters in the upper 2000 m and saltier waters below that, particularly in the Pacific and Indian Oceans. The fresh bias reaches 1.2 psu near the surface in the Indian Ocean owing to precipitation and runoff errors (for the former, see Fig. 5 of Gent et al. 2011). The largest salty biases occur in the deep Atlantic Ocean. The upper-ocean Atlantic north of 15°N remains mostly saltier than the PHC2 climatology.

We provide a comparison of the deep θ and S from CCSM4 to those of CCSM3 and PHC2, considering the θ–S diagrams given in Fig. 5. In the figure, θ and S are presented for depths >1500 m for the Southern, Pacific, Indian, Atlantic, and Labrador basins and the combined Arctic Ocean and Greenland–Iceland–Norwegian (GIN) Seas. Here, σ_2 density contours are also included. Here, the northern boundary of the Southern Ocean is 34°S; the southern and eastern boundaries of the Labrador Sea are 50°N and 46°W, respectively; and the Arctic and GIN domain includes all the ocean north of the Scotland–Iceland–Greenland line.

A prominent feature of Fig. 5 is the presence of larger than observed densities in the abyssal Southern, Pacific, Indian, and Atlantic Oceans in both CCSM3 and CCSM4. The bias is largest in the Pacific basin with 0.2 kg m^{-3}, while it is >0.1 kg m^{-3} in the other three basins. These densest waters are associated with the Antarctic Bottom Water (AABW), which forms in the Weddell and Ross Seas as well as off the continental shelves near Antarctica and then spreads northward into the abyssal plains of the Pacific, Indian, and Atlantic Oceans. In CCSM4, the denser-than-observed AABW is largely due to higher-than-observed S, whereas in CCSM3 there are contributions from both higher-than-observed S and lower-than-observed θ, producing even higher densities than in CCSM4. In both CCSM3 and CCSM4, these high salinities are likely due to excessive sea ice formation with stronger winds in the coupled simulations.

In the Southern Ocean for $\theta > 0.5$°C, the model salinities span a much larger range than in PHC2. In addition, CCSM3 shows a slight shift toward colder and fresher waters compared to those of CCSM4. In the Pacific and Indian Oceans, both CCSM3 and CCSM4 have similarly fresher and colder waters than PHC2 for $S <$ 34.7 psu with minor shifts to denser-than-observed water masses. In both basins, the AABW largely preserves its θ and S properties, suggesting little mixing with the ambient waters. Particularly in the Pacific basin, while the observational θs remain >0.5°C, the CCSM3 and CCSM4

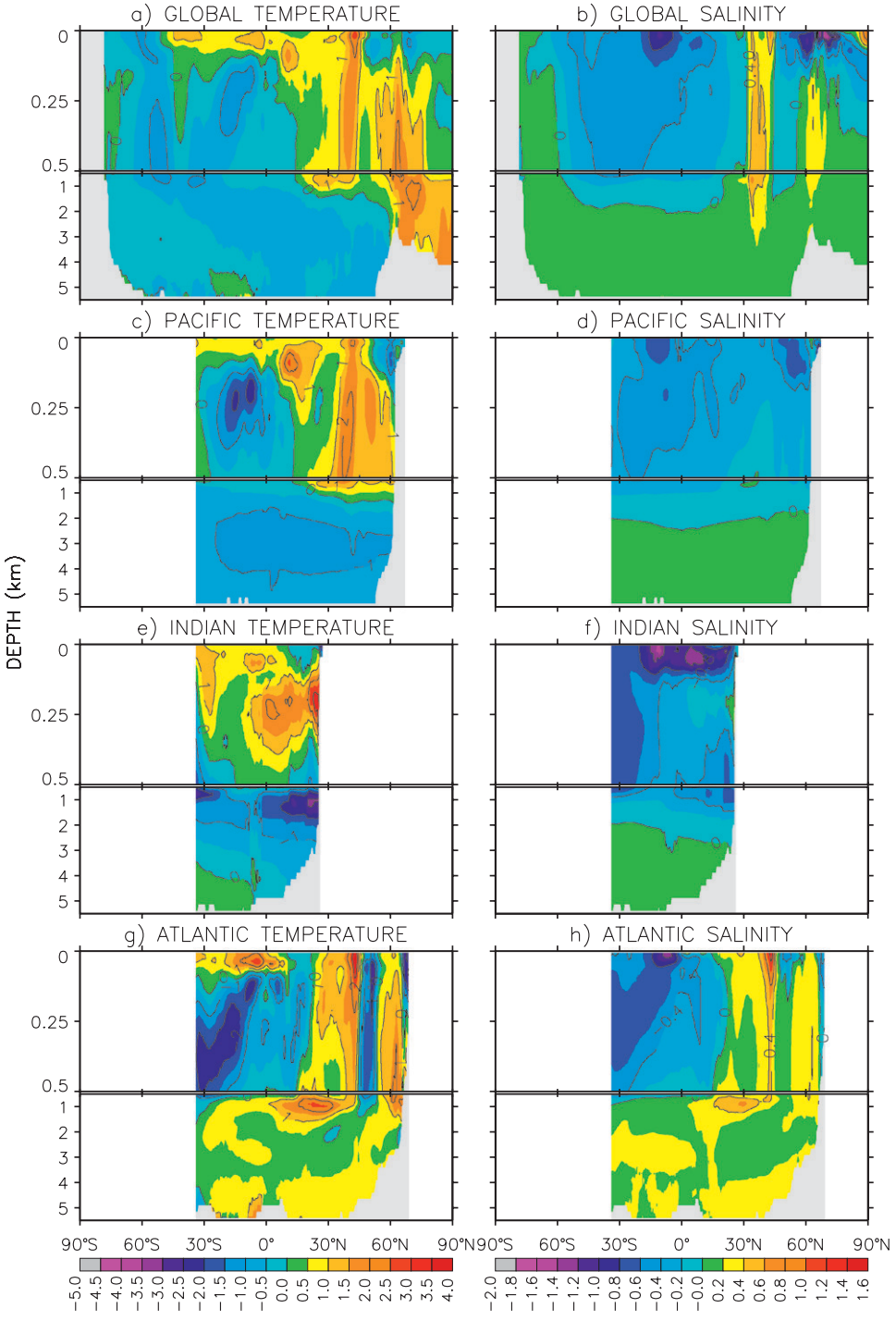

FIG. 4. Zonal-mean (left) potential temperature (°C) and (right) salinity (psu) CCSM4 minus PHC2 observations difference distributions. (top to bottom) The global, Pacific, Indian, and Atlantic Ocean differences are shown.

θs reach −1.0° and −0.25°C, respectively. In contrast with the Pacific and Indian basins, the Atlantic Ocean has warmer and saltier waters than in PHC2 in both model solutions with apparent shifts to higher density classes. Particularly in CCSM4, the North Atlantic Deep Water (NADW) is denser than in both PHC2 and CCSM3 due to its larger S, for example, in CCSM4 S is higher than in PHC2 by 0.2 psu. In the Labrador Sea, CCSM3 and

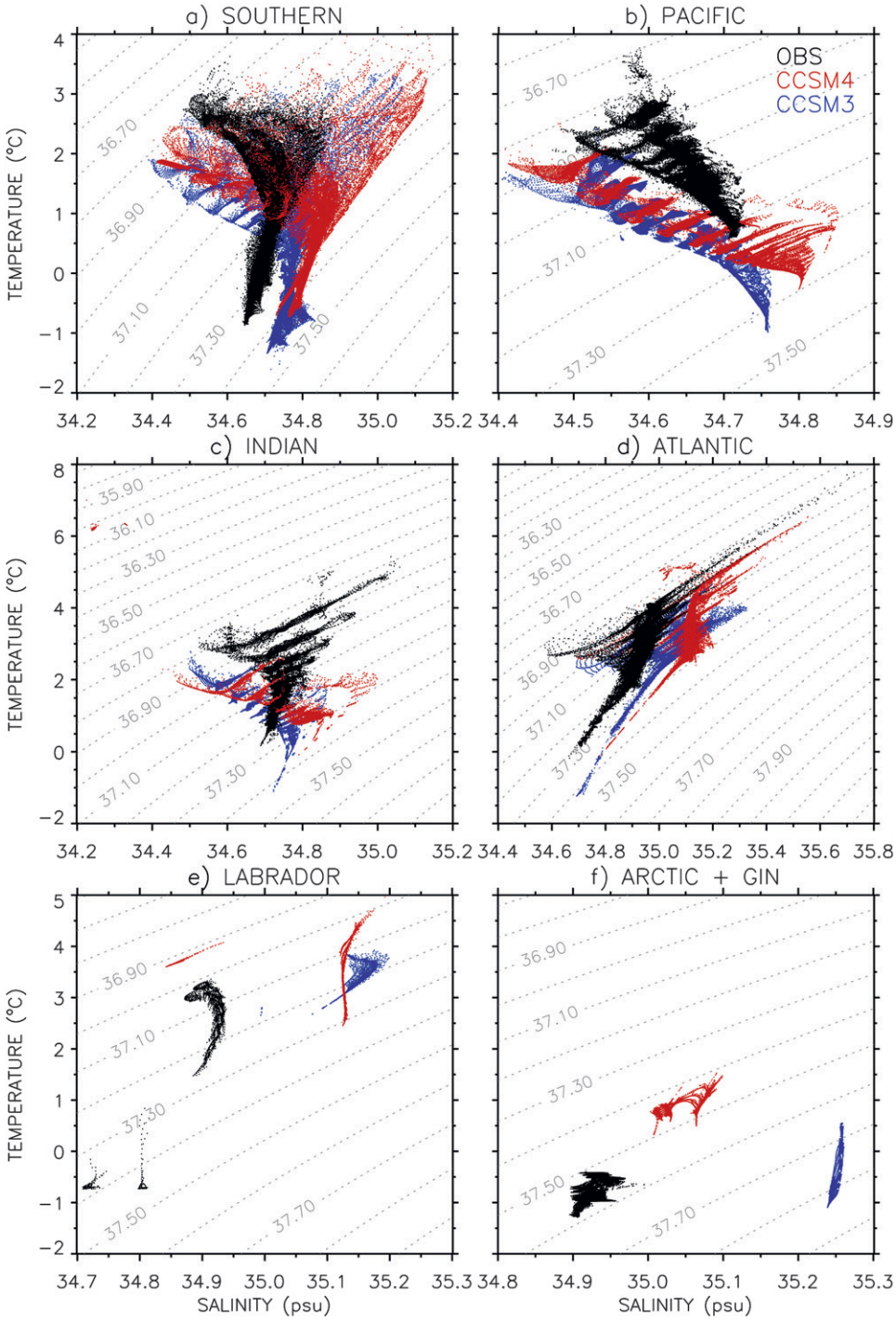

FIG. 5. Potential temperature–salinity diagrams for depths ≥ 1500 m for several ocean basins from CCSM4, CCSM3, and PHC2 observations (OBS). The σ_2 density with a contour interval of 0.1 kg m^{-3} is also shown.

CCSM4 are closer to each other than to PHC2, with both showing warmer and saltier waters but with similar densities as in PHC2. However, the vertical stratification in CCSM4 is in better agreement with PHC2 than in CCSM3 likely because of the stratifying effect of the overflow parameterization as discussed in Yeager and Danabasoglu (2012). Finally, the Arctic + GIN water masses are rather different in the models than in PHC2.

Specifically, CCSM3 is denser than in PHC2 because of its larger-than-observed S and CCSM4 is lighter than in PHC2 because of its warmer θ despite its larger S. In summary, these θ–S diagrams indicate that CCSM4 simulations have significant biases in their deep θ and S properties as in CCSM3.

b. Upper-ocean θ and S

The biases of SST and sea surface salinity (SSS) from the present-day Hurrell et al. (2008) dataset and PHC2 climatology, respectively, are shown in Fig. 6 for CCSM4, CCSM3, and OCN. An immediately apparent difference in the SST bias distributions is the generally warmer SSTs in CCSM4 than in CCSM3. Indeed, we calculate the global-mean SST biases as +0.33°C and −0.59°C in CCSM4 and CCSM3, respectively (see Table 1). The corresponding root-mean-square (rms) differences are 1.15°C for CCSM4 and 1.34°C for CCSM3. These integral measures show clear improvements in CCSM4 in comparison with CCSM3. These improvements are largely due to the different spinup procedure used in CCSM4 than in CCSM3—as detailed in Gent et al. (2011), the entire ocean, including SSTs, got colder in CCSM3 because of the significant heat loss in the preindustrial control simulation. Nevertheless, the large warm SST biases that originate in upwelling regions along the west coasts of North and South America and South Africa appear little changed in CCSM4 from CCSM3. Indeed, likely owing to the generally warmer SSTs in CCSM4, these warm bias regions are much more extensive spatially, intruding farther into the open ocean basins. Resulting from slight changes in the Gulf Stream and North Atlantic Current paths, there is a modest reduction in the magnitude of the negative North Atlantic SST bias and an increase in the warm bias off the North American coast in CCSM4. Similarly, the positive Nordic Sea bias is reduced with CCSM4, but this comes at the expense of a more extensive cold bias in the Nordic Sea. Comparing the SST bias in CCSM4 with that in OCN (mean bias = 0.06°C and rms = 0.58°C) reveals that, globally, roughly half of the rms bias and almost all of the remaining mean bias can be eliminated if the ocean model is forced with the best estimates of the natural atmospheric state. However, chronic problem regions are still apparent in the OCN SST field—upwelling regions and the Gulf Stream and its extension into the subpolar North Atlantic. As discussed in Large and Danabasoglu (2006), in addition to creating new biases, errors in coupled surface heat fluxes amplify the SST biases in these problem regions already evident in ocean-only simulations.

As in CCSM3, SSS in CCSM4 exhibits an overall fresh bias. The global mean SSS biases are very similar for CCSM4 (−0.36 psu) and CCSM3 (−0.38 psu) as shown in Table 1. The rms difference from observations indicates a modest improvement in CCSM4 compared to that of CCSM3 (0.88 psu versus 1.07 psu, respectively). In CCSM4, there is a major reduction of regions with large SSS biases of more than ±1.5 psu, identified in Large and Danabasoglu (2006) for CCSM3. Specifically, the fresh biases in the central South Pacific, northwestern Indian Ocean, and eastern South Atlantic and the saline bias in the eastern Pacific just south of Panama have been significantly reduced in CCSM4. These improvements are largely due to the reduced precipitation in the former three regions and increased precipitation in the latter in CCSM4 compared to CCSM3 (see Gent et al. 2011). We note that there are contributions also from changes in evaporation resulting from SST changes. For example, the larger warm bias in the western Indian Ocean in CCSM4 increases evaporation there. In the North Pacific, excessive precipitation becomes even larger in CCSM4, thus contributing to the change of the SSS bias from saline to fresh there. As in SST, changes in the Gulf Stream and North Atlantic Current paths reduce the fresh bias in the central North Atlantic while increasing the saline bias off the North American coast. The resulting North Atlantic is in general saltier (and denser) in CCSM4 than in CCSM3, which may partly contribute to the stronger AMOC in CCSM4 (see below). The fresh and saline biases near Congo and Amazon outflows, respectively, reflect some persistent river discharge biases in coupled CCSM simulations associated with excessive Congo and weak Amazon runoffs. Precipitation and Amazon runoff errors as well as the oceanic freshwater loss to the land model to balance the water budget over wetlands and lakes in the Eastern Caribbean are likely contributors to the saline bias in this region in CCSM4. In contrast with CCSM3, the Mediterranean in CCSM4 has now a saline bias of >3 psu. This bias is present throughout the water column and it is established during the 1850 CONTROL simulation, likely due to the lower-than-observed precipitation over the Mediterranean basin. Such low precipitation bias also existed in CCSM3, however, more realistic SSTs and the Nile discharge into the basin in CCSM4 no longer compensate for this precipitation error. We note that the Nile discharge has been reduced from 0.03 Sv (1 Sv $\equiv 10^6$ m^3 s^{-1}) in CCSM3 to 0.01 Sv in CCSM4 but still remains larger than observed (0.0013 Sv; Dai and Trenberth 2002).

In OCN, the global mean SSS bias and its rms difference are 0.07 and 0.41 psu, respectively. These smaller biases along with the spatial locations of the SSS biases in coupled simulations highlight the extent to which the coupled biases are largely associated with errors in precipitation and runoff fluxes in both CCSM4 and CCSM3. The OCN simulation has similar SSS biases as in CCSM4

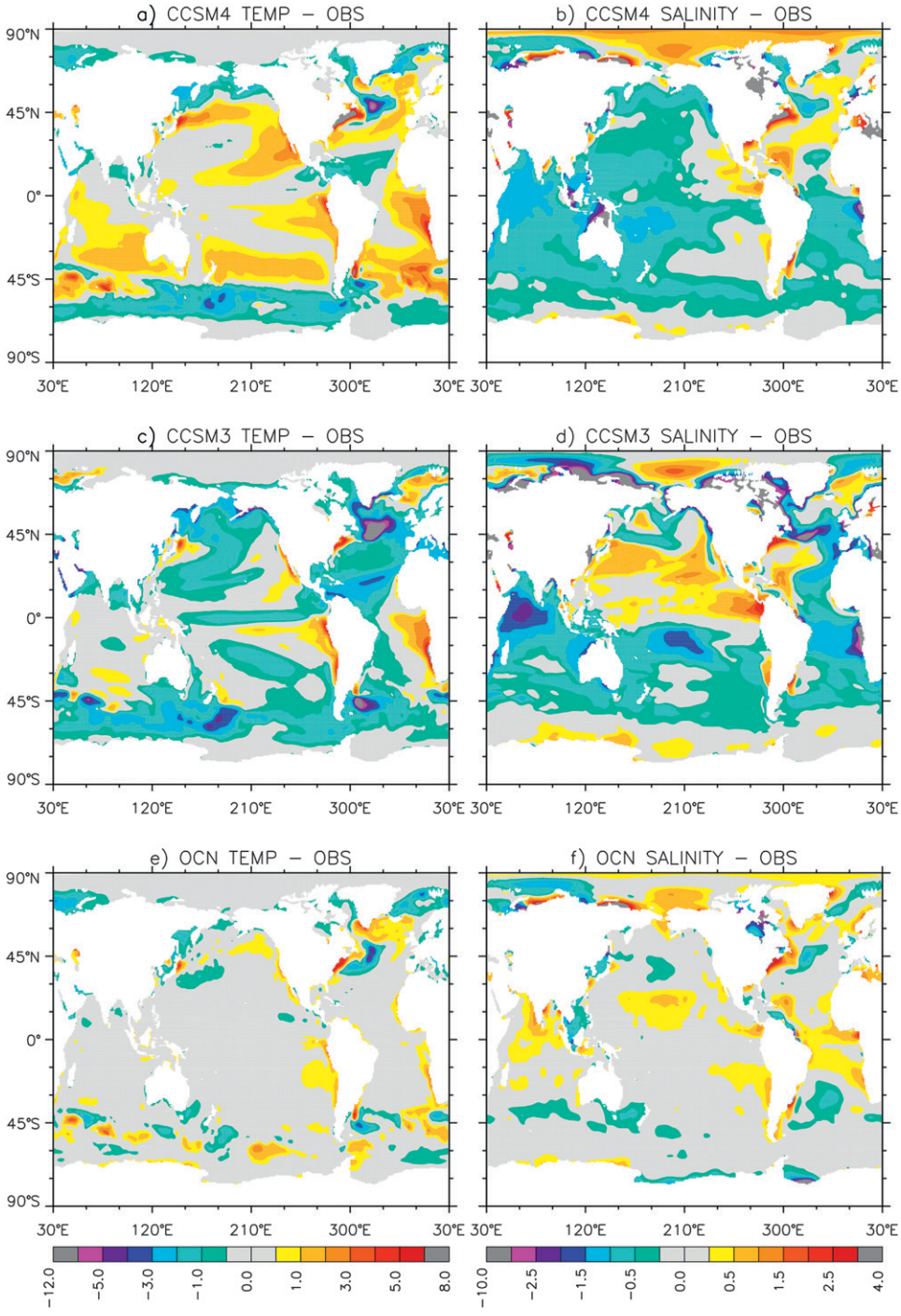

FIG. 6. (left) Sea surface temperature (°C) and (right) salinity (psu) model minus observations difference distributions. For temperature and salinity, the Hurrell et al. (2008) and PHC2 datasets are used, respectively. The differences for (top) CCSM4, (middle) CCSM3, and (bottom) OCN are shown.

in the Gulf Stream, the North Atlantic Current regions, and off the Arctic coast. In this uncoupled simulation, the only coupling between SST and SSS arises through the evaporative flux because precipitation is prescribed. Along with a weak restoring of SSS to PHC2 climatology, this partial decoupling of SST and SSS tends to reduce upper-ocean salinity biases, but it also reduces the internal consistency of the air–sea exchange in this configuration.

TABLE 1. Model minus observations mean and rms differences (biases) for SST, SSS, and global volume-mean θ and S in the upper ocean. The latter two are denoted as $\langle\theta\rangle_{1000}$ and $\langle S\rangle_{1000}$, respectively, and represent the 0–1041-m-depth range in CCSM4 and OCN and the 0–1022-m-depth range in CCSM3. The observations for SSS, θ, and S are the PHC2 dataset, while SST biases are based on the Hurrell et al. (2008) data. Temperature and salinity are in °C and psu, respectively.

	CCSM4	CCSM3	OCN
SST mean bias	0.33	−0.59	0.06
SST rms bias	1.15	1.34	0.58
SSS mean bias	−0.36	−0.38	0.07
SSS rms bias	0.88	1.07	0.41
$\langle\theta\rangle_{1000}$ mean bias	−0.09	−0.23	0.34
$\langle\theta\rangle_{1000}$ rms bias	1.27	1.66	1.11
$\langle S\rangle_{1000}$ mean bias	−0.21	−0.05	0.01
$\langle S\rangle_{1000}$ rms bias	0.52	0.45	0.20

We present the model minus PHC2 difference distributions for θ and S at about 300-m depth in Fig. 7, clearly showing significant improvements in the Pacific basin with CCSM4. Specifically, the large (both in magnitude and spatial extent), density-compensating θ and S biases of CCSM3 located in the central North and South Pacific Oceans have been mostly eliminated in CCSM4. We believe that increased vertical resolution and changes in model physics are responsible for these improvements. Elsewhere, the θ biases remain rather similar between CCSM4 and CCSM3. The rms difference of 1.34°C in CCSM4 represents a significant improvement over the CCSM3 value of 2.02°C. In S, while the Atlantic biases are similar between the two cases, the CCSM4 solutions show more extensive fresh bias regions that also include the North Indian and North Pacific basins. Consequently, the S rms differences remain similar in CCSM4 (0.54 psu) and in CCSM3 (0.48 psu). Although the cold SST bias in the North Atlantic has been reduced in CCSM4, the associated cold biases at 300-m depth are very similar in CCSM4 and CCSM3 and remain large (>7°C). We note that similar θ biases exist in OCN as in coupled cases in the high-latitude North Atlantic. The OCN rms difference of 1.25°C is only slightly better than in CCSM4, but the S rms difference of 0.20 psu in OCN is much smaller than in either coupled case.

Finally, a summary of the upper-ocean θ and S biases—both mean and rms—is given in Table 1. They represent volume averages for approximately the upper 1000-m depth. In the mean, both coupled simulations have slight cold and fresh biases, with a smaller cold bias in CCSM4 and a smaller fresh bias in CCSM3. In θ, the rms difference of 1.27°C in CCSM4 represents a modest improvement over the CCSM3 value of 1.66°C. The corresponding value in OCN is 1.11°C. Despite seemingly small mean biases in S, the rms errors remain similarly large in both coupled cases (0.52 and 0.45 psu in CCSM4 and CCSM3, respectively) compared to that of OCN (0.20 psu).

c. Parameterized overflow properties

We show the CCSM4 time series of the annual-mean parameterized volume transport M and the depth of the product water, along with those of θ and S, in Fig. 8 for the DS and FBC overflows and in Fig. 9 for the WS and RS overflows. In the overflow parameterization, all the exchanges depend on the prognostic θ and S fields that themselves depend on atmospheric forcing and ocean model physics. For example, the source and entrained water densities and, therefore, the product water density and its injection depth all depend on the evolving ambient water state. In the following discussion, we use 1986–2005 time average values to describe model overflow properties, and subscripts s and p are employed to denote source and product water properties, respectively. We note that because these θ and S values are also averages over large volumes, we do not expect them to closely match mostly local and sparse—particularly in the Southern Ocean—observational estimates.

At DS, both the source and entrained volume transports, hence the product water volume transport, increase slightly toward the end of the 20C. Here, M_s = 2.83 Sv is within the observational range of 2.6–4 Sv (Legg et al. 2009; Dickson and Brown 1994; Dye et al. 2007; Macrander et al. 2005, 2007; Girton and Sanford 2003). However, owing to low entrainment, M_p = 3.52 Sv is below the observational estimates of 3.9 Sv (Girton and Sanford 2003) and 5.2 Sv (Legg et al. 2009; Dickson and Brown 1994). In general, the DS source, entrainment, and product water θ and S get warmer and saltier, respectively, toward the end of the 20C, with compensating effects on density. The model θ_s = 1.72°C, S_s = 35.09 psu, θ_p = 2.59°C, and S_p = 35.14 psu are warmer and saltier than the observational estimates of θ_s = −0.4–0.7°C, S_s = 34.81 psu, θ_p = 2.1°C, and S_p = 34.84 psu (Legg et al. 2009; Macrander et al. 2005, 2007). The product water is injected at a depth of 1969 m consistent with an observational estimate of 1600 m (Legg et al. 2009). We note that the product water injection depths remain constant at all parameterized overflow sites throughout the 20C with very little ensemble spread.

In comparison with DS, the trends in the FBC properties remain rather modest. The FBC M_s = 1.82 Sv is within the observational range of 1.5–3.5 Sv (Legg et al. 2009; Dye et al. 2007; Mauritzen et al. 2005). As in DS, the entrainment transport is low, resulting in M_p = 2.09 Sv, which is below the observational range of 2.5–4.2 Sv (Legg et al. 2009; Mauritzen et al. 2005). While θ_s = 2.39°C and S_s = 35.15 psu are much warmer and saltier

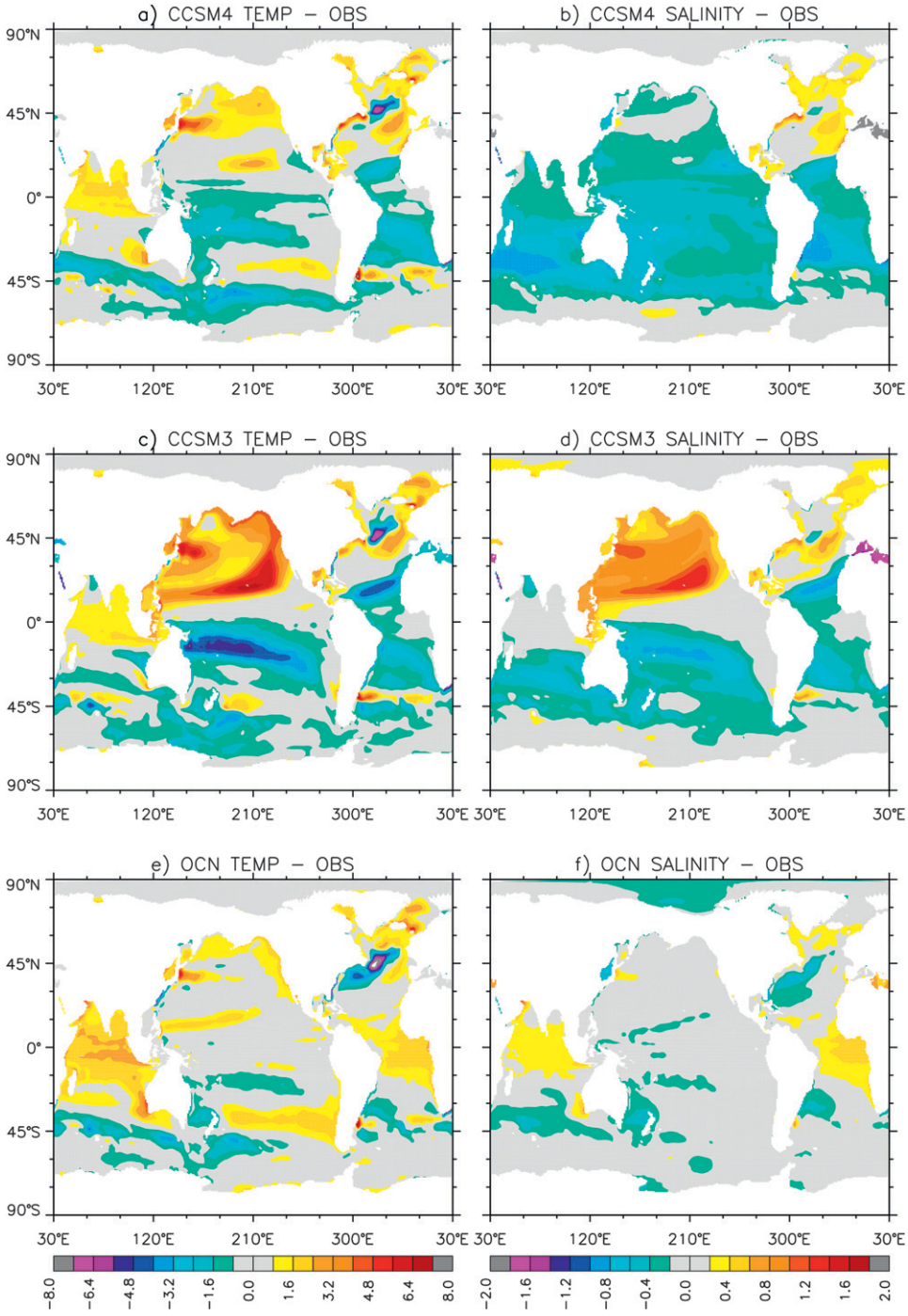

FIG. 7. (left) Potential temperature (°C) and (right) salinity (psu) model minus PHC2 climatology (OBS) difference distributions at a depth of 305 m for CCSM4 and OCN and 318 m for CCSM3. The differences for (a),(b) CCSM4, (c),(d) CCSM3, and (e),(f) OCN are shown.

than the observational estimates ($\theta_s = 0$°C, $S_s = 34.92$ psu; Legg et al. 2009), the product water $\theta_p = 3.09$°C and $S_p = 35.20$ psu are in better agreement with the broad observational ranges of 0°–6°C and 34.9–35.15 psu (Mauritzen et al. 2005). The FBC product water is injected at a depth of 2187 m, shallower than the observational estimate of 3000 m (Legg et al. 2009). The combined DS and FBC product water volume transport reaches 5.61 Sv.

In contrast with the DS and FBC overflows in which dense waters form behind a topographic barrier, the WS

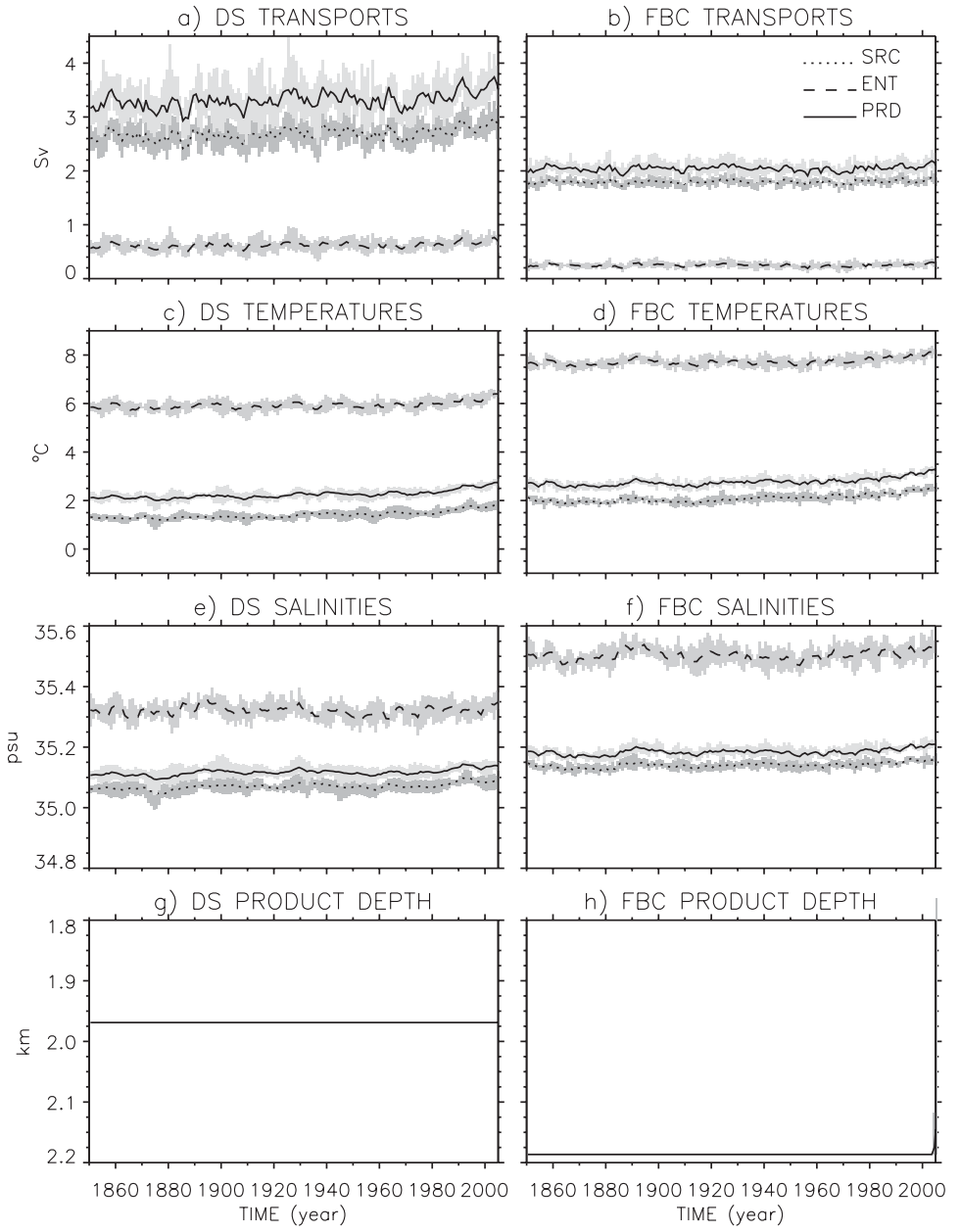

FIG. 8. Time series of the annual-mean (left) DS and (right) FBC overflow properties from CCSM4 simulations: (a),(b) volume transports, (c),(d) potential temperatures, (e),(f) salinities, and (g),(h) product water depth. The source (SRC), entrainment (ENT), and product (PRD) properties are shown. The lines represent the CCSM4 ensemble means and shading indicates the ensemble spread.

and RS overflows represent the overflow of dense waters formed over continental shelves. Because of the lack of a well-defined channel or strait, some choices in the parameterization, for example, placement of the source region and sills, remain necessarily arbitrary for these overflows (see Briegleb et al. 2010). Furthermore, assessing the fidelity of the overflow parameterization is challenging because of the rather poor temporal and spatial coverage of any observational data in these regions. Figure 9 shows that the parameterized overflow transports are rather anemic in comparison with the North Atlantic overflows, particularly in the WS. Throughout the simulations, there is little to no entrainment, and by the end of the 20C, there is virtually no product water transport, that is, $M_p = 0.008$ Sv. Although rather poor, the observational estimates are $M_s = 1$ Sv and $M_p = 5$ Sv

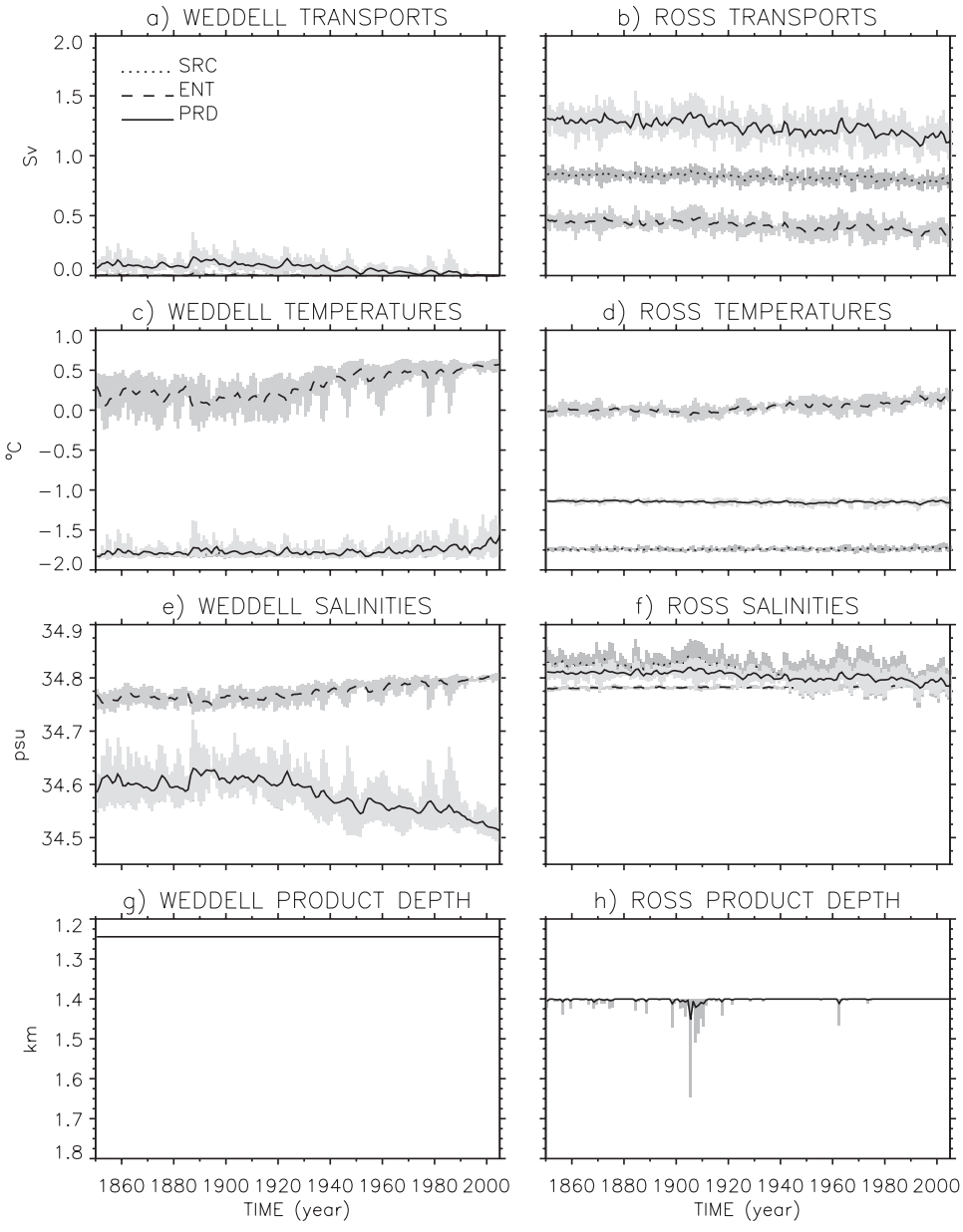

FIG. 9. As in Fig. 8, but for the Weddell and Ross Sea overflows.

(Legg et al. 2009; Foldvick et al. 2004). In the WS source region, we calculate $\theta_s = -1.69$°C and $S_s = 34.53$ psu, and speculate that these warmer and fresher than observed values ($\theta_s = -1.9$°C and $S_s = 34.67$ psu; Legg et al. 2009) along with the density of the ambient waters in the ocean interior and in the entrainment region contribute to the weaker WS transports.

At the RS overflow, $M_s = 0.79$ Sv and $M_p = 1.15$ Sv compare much more favorably with the observational estimates of $M_s = 0.6$ Sv and $M_p = 2$ Sv (Legg et al. 2009; Gordon et al. 2004). Again, there is a low bias in M_p with observations due to low entrainment in the model despite larger model M_s. We calculate $\theta_s = -1.73$°C, $S_s = 34.80$ psu and $\theta_p = -1.15$°C, $S_p = 34.79$ psu, all comparing well with their observational counterparts of $\theta_s = -1.9$°C, $S_s = 34.8$ psu and $\theta_p = -1.0$°C, $S_p = 34.72$ psu. Among all the parameterized overflows, the RS product water injection depth is the only one with some noticeable variability both in time and among the ensemble members with a mean depth of 1400 m. This is shallower than the observational estimate of >3000 m (Legg et al. 2009).

d. *Meridional overturning circulation and heat transports*

We present the time-mean global and Atlantic meridional overturning circulation distributions in Fig. 10. For CCSM4 and OCN, these are for the total flow, that is, the Eulerian-mean and parameterized mesoscale and submesoscale eddy contributions are all included. The CCSM3 distributions are for the Eulerian-mean velocity only because the mesoscale eddy contribution was not explicitly calculated, and the submesoscale parameterization was not used in CCSM3. The seemingly largest discrepancy between CCSM4 and CCSM3 occurs in the strength of the cell at the latitudes of the Antarctic Circumpolar Current (ACC). This is simply due to the fact that this cell represents the residual circulation, that is, the sum of the Deacon Cell and the parameterized eddy contributions, in CCSM4 in contrast to just the Deacon Cell in CCSM3. Indeed, a comparison of the Deacon Cells from CCSM4 and CCSM3 with maximum transports of >40 and >48 Sv, respectively, reveals much smaller differences between the two cases (not shown). The second largest difference between CCSM4 and CCSM3 is the weaker AABW (counterclockwise circulation below about 3000-m depth, as displayed in Fig. 10) transport in CCSM4 (about 8 Sv global) than in CCSM3 (>16 Sv global). This weaker CCSM4 transport appears to be at the low end of the production rate–based observational estimates of 8.1 $\pm$2.6 Sv (Orsi et al. 2002) and 8–12 Sv and 5–15 Sv (Orsi et al. 1999 and references therein). Similarly, the AABW maximum transport in the Atlantic Ocean is smaller in CCSM4 (2.9 Sv) than in CCSM3 (6.1 Sv). The cell associated with the NADW (clockwise circulation in the Atlantic Basin, as displayed in Fig. 10) is similar in both, but its maximum transport is larger in CCSM4 than in CCSM3 (24 versus 21 Sv, respectively). Because of the OFP, the NADW penetration depth—as measured by the depth of the zero streamline separating the NADW and AABW cells—is deeper in CCSM4 than in CCSM3 north of 30°N. South of this latitude, the NADW is deeper by only a few hundred meters in CCSM4 than in CCSM3 (see below). In general, the circulation patterns and maximum transport magnitudes are very similar between CCSM4 and OCN, including the NADW and AABW. The NADW penetration depth is 300–400 m deeper in OCN than in CCSM4 south of 30°N.

A quantitative comparison of the model AMOC profiles with the profile based on the Rapid Climate Change (RAPID) mooring array data (Cunningham et al. 2007) at 26.5°N is provided in Fig. 11. Again, the CCSM3 profile is for the Eulerian-mean component only, but the eddy contributions are very small at this latitude. These profiles represent the total integrated transport between the surface and a given depth, with negative and positive slopes showing northward and southward flows, respectively. As indicated above, the penetration depth of the NADW remains rather shallow with a mean depth of about 3250 m in CCSM4 despite the overflow parameterization. A major reason for this is that the DS and FBC overflow product waters cannot penetrate much deeper south of 30°N because of the denser waters in the North Atlantic, resulting primarily from a salty bias in excess of 0.2 psu at depth as shown in Fig. 4h. Consequently, in comparison with CCSM3, the CCSM4 simulations do not show any improvements in the NADW penetration depth at this latitude. This lack of improvement in the CCSM4 20C simulations is in contrast with two sets of CCSM4 present-day simulations discussed in Danabasoglu et al. (2010) and Yeager and Danabasoglu (2012), which show deeper NADW penetration depths with the OFP. In both CCSM3 and CCSM4, the AABW is shallower than in the RAPID data with weaker transports in CCSM4 than in CCSM3. In OCN, the flow is rather weak between 3500 m and the ocean bottom with a zero-crossing depth of 4500 m consistent with the RAPID profile. However, in contrast with observations, the AABW is largely missing in OCN at 26.5°N as in the simulations of Danabasoglu et al. (2010). The maximum northward transports across 26.5°N are 18.0, 18.4, and 18.7 Sv in CCSM4, OCN, and CCSM3, respectively, occurring at about 1000-m depth. All these model transports compare very favorably with the corresponding RAPID mean transport estimate of 18.7 Sv, and they are certainly within the interannual range of the RAPID estimates.

Figure 12 presents the global and Atlantic Ocean northward heat transports (NHT) from CCSM4, CCSM3, and OCN in comparison with the implied transport estimates from Large and Yeager (2009) calculated using the CORE interannual fluxes for the 1984–2006 period and with an Atlantic Ocean estimate based on the RAPID data from Johns et al. (2011). The figure shows that the ensemble spread in NHT in CCSM4 simulations is rather small. While the maximum global NHT of 1.82 PW in CCSM4 is within the implied estimate range, it is smaller than the CCSM3 maximum NHT of 2.01 PW; the maximum transport in OCN (1.62 PW) remains below the estimate range. In comparison with Large and Yeager (2009), all cases transport less heat northward between 0° and 10°N and more heat southward between 20°S and 0°. In all cases, the peak southward transports are displaced by about 10° northward to 15°S, indicating that the net surface heat loss in model simulations occurs in lower latitudes than the estimates suggest. South of 20°S, the model southward transports remain larger than the implied estimates with slightly better agreement with

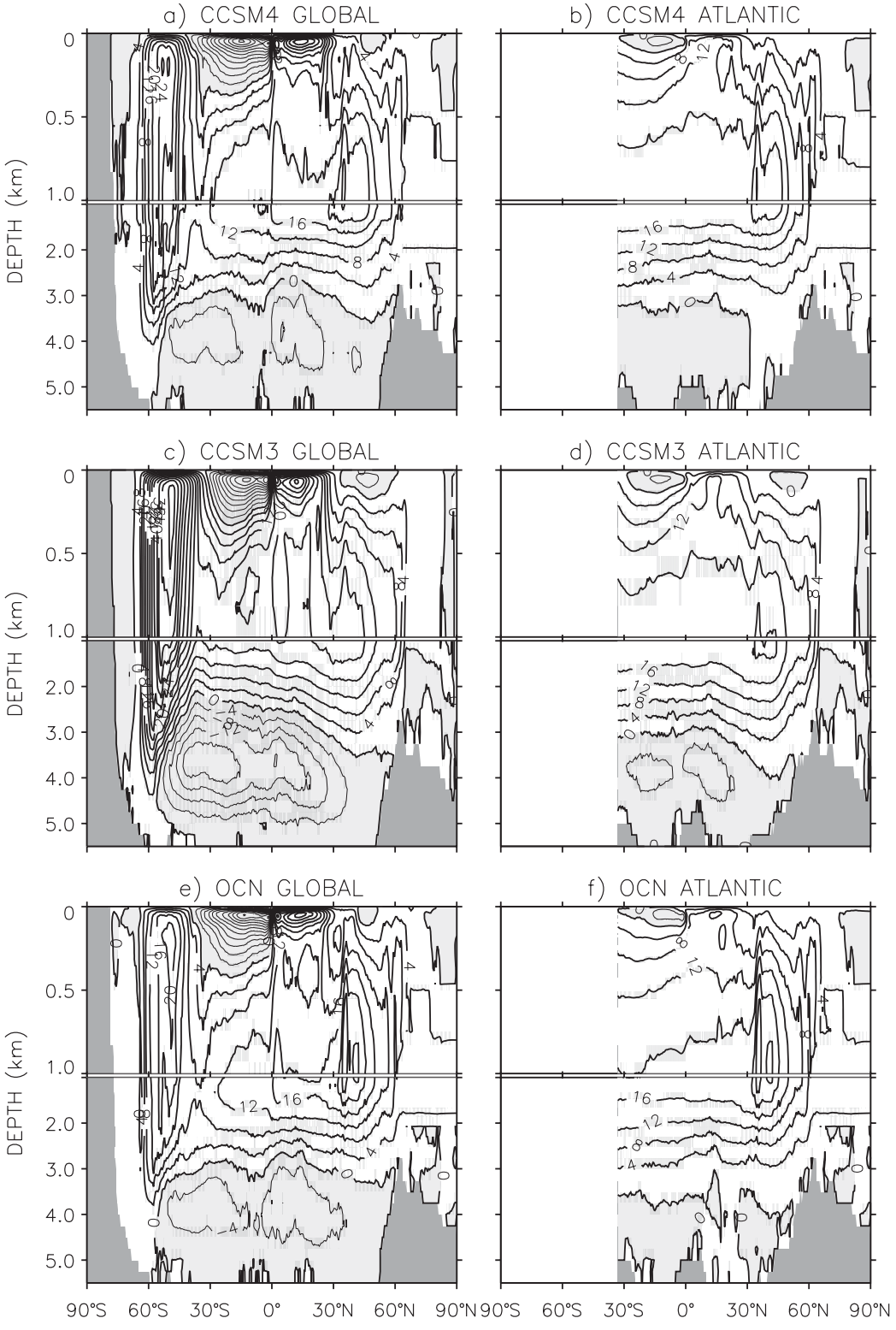

FIG. 10. Zonally-integrated meridional overturning circulations for the (left) global and (right) Atlantic Oceans from (top to bottom) CCSM4, CCSM3, and OCN. The CCSM4 and OCN transports include the Eulerian-mean and parameterized mesoscale and submesoscale contributions. The CCSM3 transports are for the Eulerian-mean component only. The positive and negative (shaded regions) contours denote clockwise and counterclockwise circulations, respectively. The contour interval is 4 Sv.

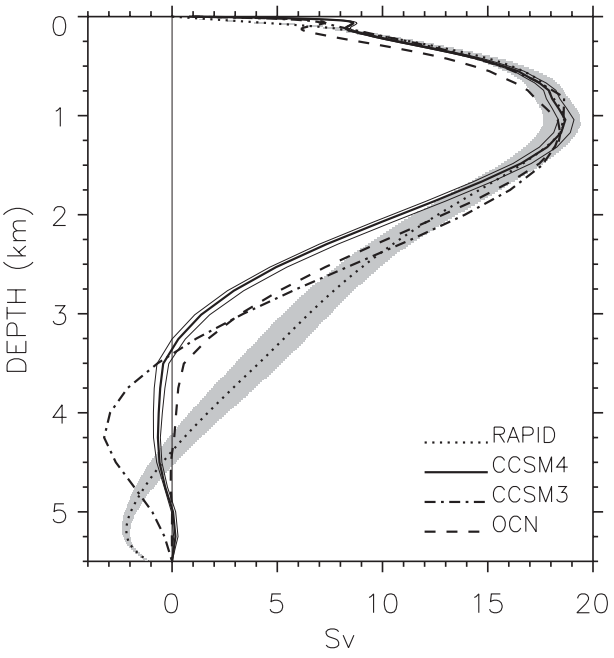

FIG. 11. Atlantic meridional overturning circulation profiles at 26.5°N from CCSM4, CCSM3, and OCN in comparison with the 4-yr mean RAPID data (April 2004–April 2008). Profiles represent yr 1986–2005 and yr 2004–07 means for CCSM4 and OCN, respectively, and they are for the total flow. The CCSM3 profile is for the Eulerian-mean component only and represents time-mean for yr 1980–99 for the ensemble mean of eight CCSM3 simulations. The shading indicates the interannual variability range in the annual-mean RAPID data over the four years. The thin solid lines around the CCSM4 line show the minimum and maximum ranges of the ensemble spread.

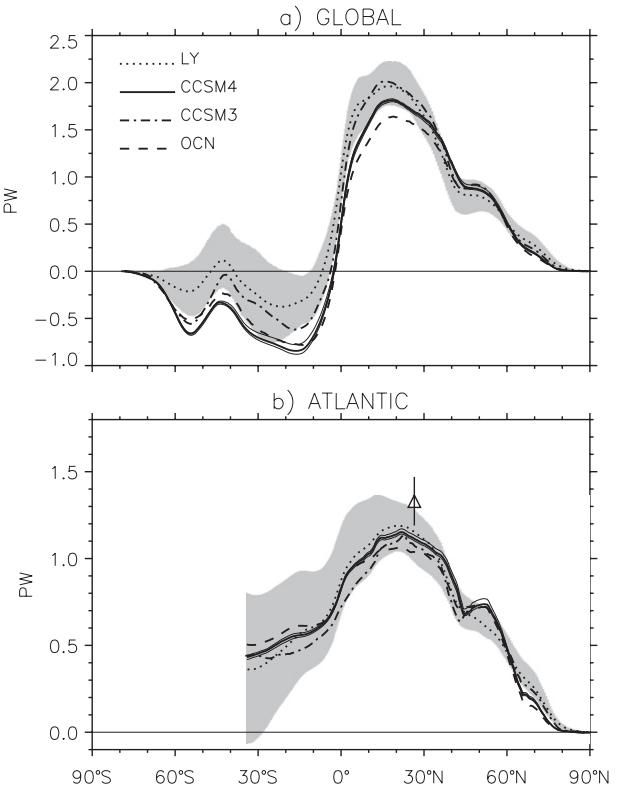

FIG. 12. (a) Global and (b) Atlantic Ocean northward heat transports. The global transports are the total transports, including the parameterized mesoscale, submesoscale (only in CCSM4 simulations), and diffusive contributions. The Atlantic Ocean transports for CCSM4 and OCN exclude the diffusive component while the corresponding CCSM3 transport is for the Eulerian-mean component only. The dotted line denoted by LY represents implied time-mean transport calculated by Large and Yeager (2009) with shading showing the implied transport range in individual years. The thin solid lines around the CCSM4 line show the minimum and maximum ranges of the ensemble spread. The triangle with the error bar is an estimate based on the RAPID data from Johns et al. (2011).

them in CCSM3. Most of the global NHT occurs in the Atlantic basin. In general, the model NHTs are within the Large and Yeager (2009) range with maximum transports of 1.06, 1.14, and 1.15 PW in OCN, CCSM3, and CCSM4, respectively. We note that in all cases the NHT remains outside of the RAPID estimate range at 26.5°N.

e. Barotropic transports

We show the barotropic (vertically integrated) streamfunction distributions from CCSM4 in comparison with CCSM3 and OCN in Fig. 13. Here, we primarily highlight some of the main differences between CCSM3 and CCSM4 and for further details refer to Large and Danabasoglu (2006) in which CCSM3 present-day control transports are discussed and compared to available observational estimates. We note that the CCSM3 barotropic transport magnitudes and their distributions given in Fig. 13b are very similar to those of the present-day CCSM3 shown in that study. In general, Fig. 13 shows that, while the coupled model transports are larger than in OCN, the CCSM4 transports are somewhat weaker than in CCSM3. In comparison with CCSM3, the most prominent improvement in CCSM4 occurs in the ACC transport through Drake Passage (DPT). Specifically, DPT has been reduced from 204 Sv in CCSM3 to 172 Sv in CCSM4 (Table 2). The inferred source of the remaining bias with the observational estimate of 137 ±8 Sv (Cunningham et al. 2003) is still the coupled surface forcing, rather than the ocean model physics because DPT = 142 Sv in OCN is within the observed range. The zonal-mean zonal wind stress τ_x from CCSM3 and CCSM4 is presented in Fig. 14 in comparison to τ_x from the CORE atmospheric datasets used in OCN. In comparison with CCSM3, the peak τ_x magnitude is about 10% smaller and its location is shifted southward in CCSM4. However, the CCSM4 τ_x maximum is still much larger than in observations (by >30%). Therefore, we believe that the >30-Sv

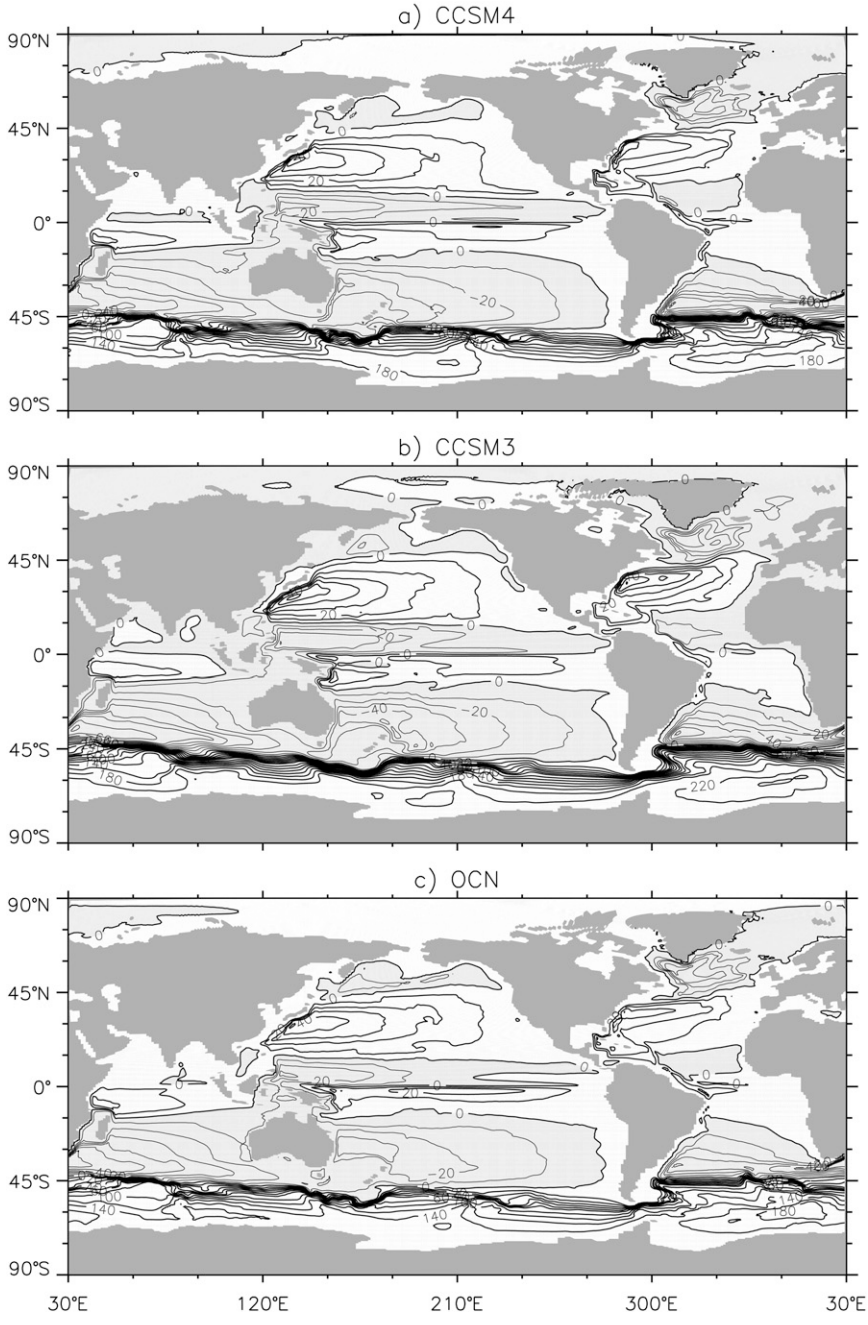

FIG. 13. Barotropic streamfunction from (a) CCSM4, (b) CCSM3, and (c) OCN. The contour intervals are 10 and 20 Sv for transports smaller and greater than 60 Sv, respectively. The thick and thin (shaded regions) lines denote clockwise and counterclockwise circulations, respectively.

reduction in DPT in CCSM4 compared to that of CCSM3 is mainly due to the reduced horizontal viscosities as discussed in Jochum et al. (2008), however, detailed mechanisms for this counterintuitive behavior are not fully understood.

In the North Atlantic, the subpolar gyre maximum transports are very similar in both CCSM3 and CCSM4. However, as evidenced by the warmer SSTs (Fig. 6) and reduced sea ice extent in the Labrador Sea region—particularly the latter represents better agreement with observations (Holland et al. 2012)—changes due to the reduced horizontal viscosities produce a warmer and stronger boundary current entering the Labrador Sea

TABLE 2. Comparison of model barotropic transports with the observational estimates given in section 3e. The transports are for FCT, the Antarctic Circumpolar Current transport through the Drake Passage (DPT), the ITF, BST, and the MCT. They are in Sv.

	CCSM4	CCSM3	OCN	Observed
FCT	28	27	27	25 ±1
DPT	172	204	142	137 ±8
ITF	12	16	11	11.6–15.7
BST	0.96	0.96	0.67	0.83 ±0.5
MCT	15	22	15	5–26

as detailed in Jochum et al. (2008). The Gulf Stream maximum transport is further reduced by >10 Sv in CCSM4 than in CCSM3, and there is a slight northward displacement of the Gulf Stream separation location and its immediate subsequent path because of the overflow parameterization as discussed in Danabasoglu et al. (2010)—see also Yeager and Jochum (2009) for other factors affecting the Gulf Stream path. Consequently, the warm SST bias just off the North American coast is warmer in CCSM4 than in CCSM3, and the cold bias in the midlatitude North Atlantic has been reduced (Fig. 6). As shown in Table 2, both the ITF and Mozambique Channel (MCT) transports are lower in CCSM4 (12 and 15 Sv, respectively) than in CCSM3 (16 and 22 Sv, respectively). The observational ranges are 11.6–15.7 Sv for ITF (Gordon et al. 2010) and 5–26 Sv for MCT (DiMarco et al. 2002). Thus, both CCSM4 and CCSM3 ITF and MCT are in agreement with the broad observational ranges. In OCN, while MCT = 15 Sv is within the observational estimate, ITF = 11 Sv is a little lower than in observed. We calculate the transports between Florida and Cuba (FCT) as 28, 27, and 27 Sv in CCSM4, CCSM3, and OCN, respectively, which are only slightly higher than the observational estimate of 25 ±1 Sv from Hamilton et al. (2005). Finally, the Bering Strait transports (BSTs) of 0.96, 0.96, and 0.67 Sv from CCSM4, CCSM3, and OCN, respectively, are all within the observed range of 0.83 ±0.5 from Roach et al. (1995). We note that the more-than-double South Atlantic subtropical gyre transport bias compared to observations identified in Large and Danabasoglu (2006) for CCSM3 remains in CCSM4. In general, the lower horizontal viscosities in CCSM4 produce somewhat tighter western boundary currents, but they remain necessarily sluggish because of the coarse model resolution.

f. Equatorial Pacific

Zonal currents in the Pacific Ocean along the equator and at 110°W from model solutions are compared to the observational distributions from Johnson et al. (2002) in Fig. 15. At 110°W, there are significant improvements in the equatorial current structure with CCSM4, providing a much better comparison with observations than in CCSM3. Specifically, the Equatorial Undercurrent (EUC) is narrower in its north–south extent and penetrates deeper; the below-surface structure of the South Equatorial Current (SEC) is better defined with narrow bands of westward flow on both sides of the EUC; and there is

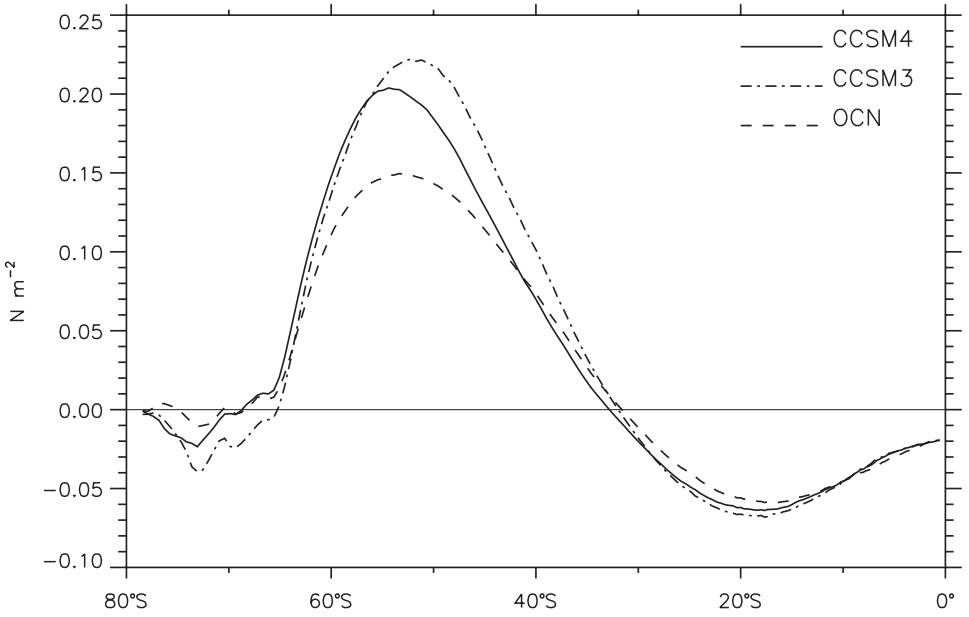

FIG. 14. Zonal-mean zonal wind stress from CCSM4, CCSM3, and OCN. OCN represents the observed wind stress forcing used in the CORE atmospheric datasets.

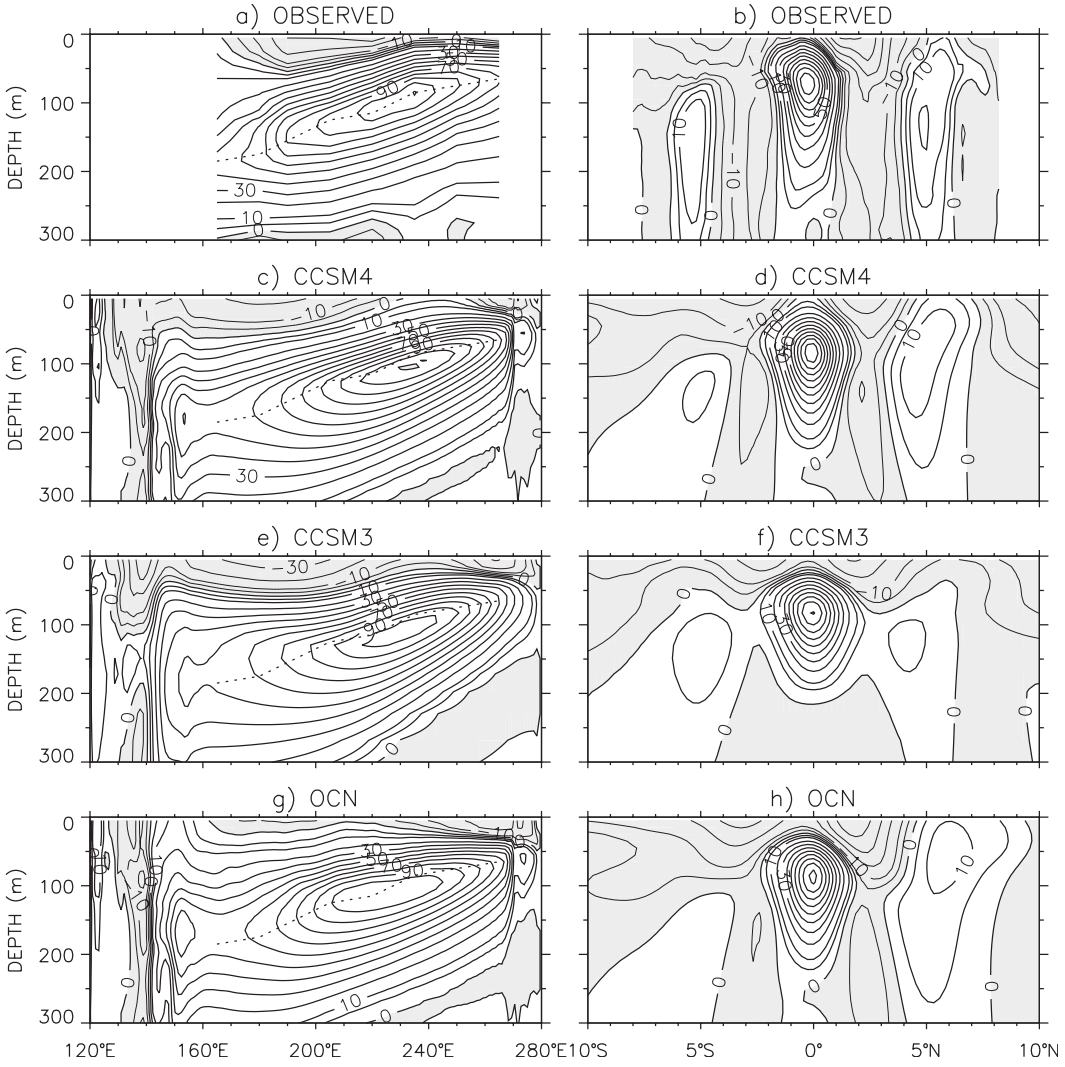

FIG. 15. Zonal velocity in the Pacific Ocean along (left) the equator and at (right) 110°W. (a),(b) The observations are from Johnson et al. (2002). The regular contour interval is 10 cm s^{-1}, but ± 5 cm s^{-1} contour lines are also drawn. The westward flow regions (thin lines) are shaded. (c),(e),(g) The depth of the maximum eastward velocity from observations is shown by the dotted trace.

a stronger and better defined North Equatorial Counter Current (NECC) at about 5°N. All these improvements are present also in OCN. The first two of the improvements are due to up to two orders of magnitude reductions in the horizontal viscosities in CCSM4 compared to those of CCSM3 (see Jochum et al. 2008). The strengthening of the NECC is due to the improved trade winds (Neale et al. 2008), resulting in an improved wind stress curl that forces this current (Sverdrup 1947). Both observations and OCN show an asymmetric SEC, with stronger westward flow north of the equator. This asymmetry is only weakly present in both CCSM4 and CCSM3, likely due to the more symmetric-than-observed wind and precipitation forcing problems in these coupled simulations.

Along the equator, the core depth (defined as the depth of the maximum eastward zonal velocity) and strength of the EUC are well represented in all model solutions. West of 200°E, the modeled core depths are shallower than in observations, but CCSM4 and OCN are in better agreement with observations. For example, at 180°, we find 165, 165, 150, and 175 m as the core depths in CCSM4, OCN, CCSM3, and observations, respectively. In contrast, east of 200°E, the modeled core depths are generally deeper than in observations with similar depths in CCSM4 and CCSM3. For example, at 110°W, the core depths are 85, 85, and 83 m in CCSM4, OCN, and CCSM3, respectively, compared to 75 m in observations. So, the tilt of the EUC core is slightly flatter in model solutions

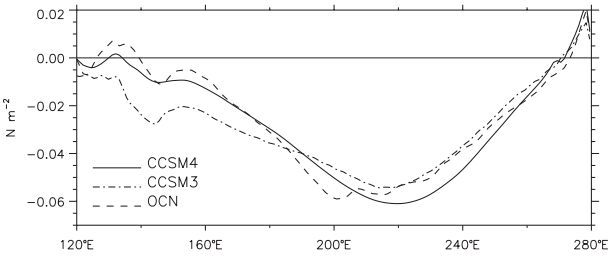

FIG. 16. Zonal wind stress along the equatorial Pacific from CCSM4, CCSM3, OCN. The OCN represents the observed wind stress forcing used in the CORE atmospheric datasets.

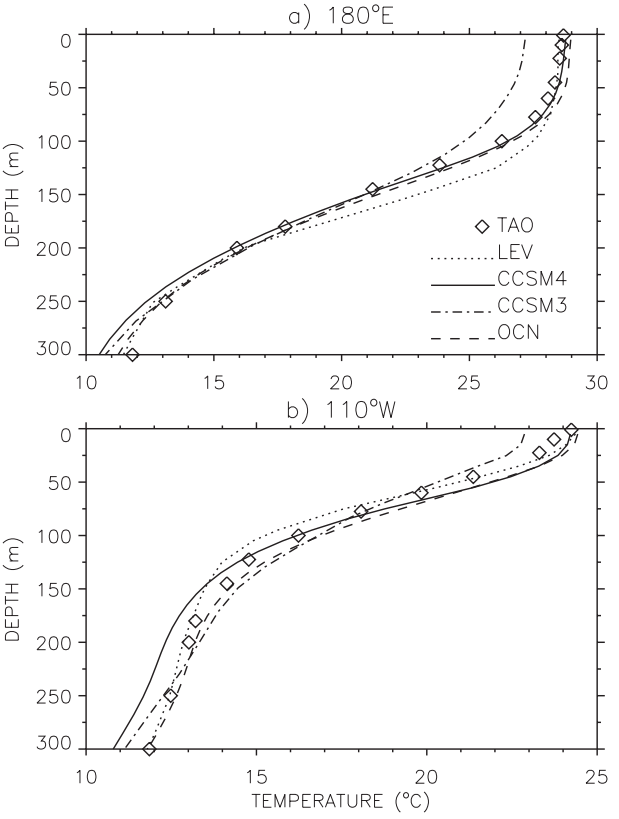

FIG. 17. Potential temperature on the equator at (a) 180° and (b) 110°W from CCSM4, CCSM3, and OCN. The diamonds indicate the observations based on the mean TAO mooring data. The dotted line labeled as LEV shows the potential temperature based on Levitus et al. (1998).

than observed. The maximum EUC speeds are 122, 107, and 110 cm s^{-1} in CCSM4, CCSM3, and OCN, respectively. The corresponding observational value is 110 cm s^{-1}. Thus, the maximum speed is about 10% larger in CCSM4 than in both observations and other model cases. Jochum et al. (2008) show a >10% increase in the maximum EUC speed with reduced horizontal viscosities. With the same horizontal viscosity prescription as in CCSM4, but forced with observed wind stress (Fig. 16), OCN shows a maximum EUC speed identical to that of observations. Therefore, we believe that this bias in CCSM4 is directly related to the local wind stress biases as the local zonal wind stress is the other major factor that determines the EUC speed (McCreary 1981). While the maximum westward wind stress in CCSM4 is almost identical to the observed stress, that is, that of OCN, the location of the maximum is shifted east from 200°E in OCN to 220°E. A similar shift also occurs in CCSM3. However, in contrast with CCSM3, the westward wind stress is generally stronger in CCSM4 than in both CCSM3 and OCN east of about 210°E. To the west of the date line, the westward wind stress is weaker in CCSM4 than in CCSM3, producing accordingly weaker surface westward flow. Finally, we note that in both CCSM4 and OCN, the EUC weakens abruptly at about 270°E due to the presence of the Galapagos Islands in the new model configuration (Fig. 15).

Figure 17 presents the model θ profiles at the equator at 180° and 110°W in comparison with the observational data from the Tropical Atmosphere Ocean (TAO) array (e.g., McPhaden et al. 1998). At both locations near the surface, CCSM4 and OCN show good agreement with the TAO data and the elimination of the cold bias that was present in CCSM3. This improvement is likely due to the lower horizontal viscosities that allow for more vigorous tropical instability waves (Jochum et al. 2008) whose meridional heat transports remove the cold bias of the equatorial cold tongue (Hansen and Paul 1984; Jochum et al. 2005). As particularly evident at 110°W, the CCSM4 thermocline remains nearly as sharp as in observations, in contrast with a more diffuse thermocline in CCSM3. Three main changes to the ocean model primarily accounted for this improvement and all three contributed about equally to the sharpening of the thermocline and the lifting of the EUC core in the west: stratification dependent isopycnal and thickness diffusivities, increase of vertical resolution, and reduction of background diapycnal diffusivity. A persistent coupled model bias is the subthermocline waters that are >1°C colder than in observations in both CCSM4 and CCSM3. We believe that this bias can be partly attributed to the atmospheric forcing errors. The subthermocline waters are mostly supplied from the Subantarctic South Pacific (e.g., Toggweiler et al. 1991) whose surface properties have a cold and fresh bias (Fig. 6) because of the overly strong Southern Hemisphere storm track. These surface properties are subducted and advected adiabatically to the equator where they likely lead to the biases seen in Fig. 17. Finally, we note that the Levitus et al. (1998) dataset is misleading along the equator. The semigeostrophic nature of the EUC means that the isotherms are pulled

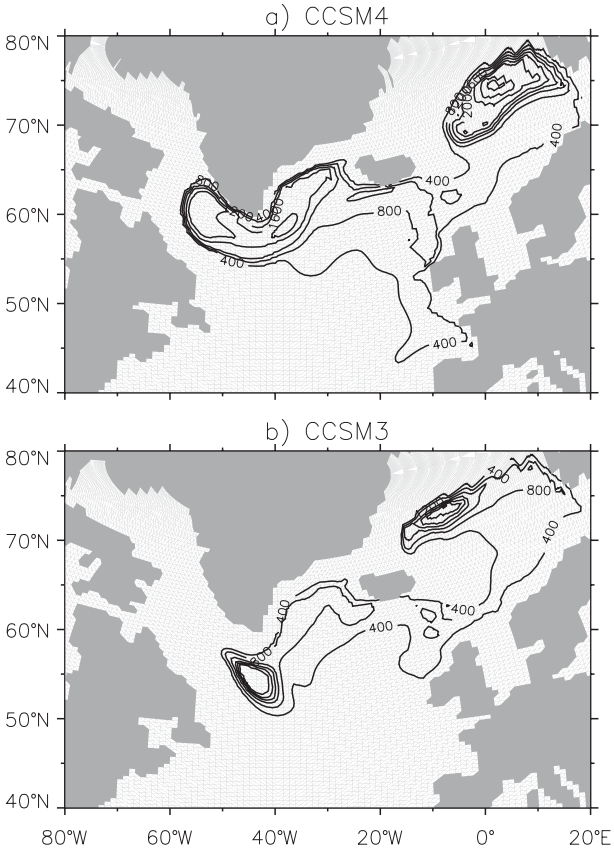

FIG. 18. Winter-mean (January, February, and March) mixed layer depth in the northern North Atlantic from (a) CCSM4 and (b) CCSM3. The contour interval is 400 m.

up above the EUC core and pushed down below it. Meridional smoothing of hydrographic sections across the equator will then lead to warming above the core, and cooling below it, thereby producing an overly sharp thermocline particularly evident at 110°W (Fig. 17, dotted line).

g. Mixed layer depth

We first highlight changes in the Labrador Sea deep water formation sites with CCSM4, considering the winter-mean mixed layer depth (MLD) distributions given in Fig. 18. Using monthly-mean potential density (referenced to surface), MLD is calculated as the depth at which potential density changes by 0.125 kg m^{-3} from its surface value. The local MLD maximum is located slightly southeast of Cape Fairwell in CCSM3. In contrast, the local MLD maximum occurs in the central Labrador Sea in CCSM4, providing a much improved comparison with observational estimates of deep convection locations (Lavender et al. 2002). This improvement appears to be mostly due to the OFP in coupled simulations (see also Yeager and Danabasoglu 2012). The ocean-only cases forced with observed atmospheric datasets produce MLD distributions very similar to that of CCSM4 regardless of whether the Nordic Sea overflows are parameterized or not. Thus, the OFP likely compensates for other coupled model errors, i.e., those of surface forcing. We note that the deepest MLDs with >3200 m in CCSM4 and >2800 m in CCSM3 occur in the GIN Seas along the ice edge. The changes in their locations reflect the changes in ice extents between CCSM3 and CCSM4.

A global view of model winter-mean MLD distributions is provided in Fig. 19 in comparison with the estimates based on the PHC2 data. The model minus observations difference distributions are similar in their gross features for all cases, with their largest departures from the PHC2-based estimate occurring in regions of relatively poor observational data, i.e., the Southern Ocean and northern North Atlantic. In details, CCSM4 and OCN MLDs look more alike than in CCSM3. We calculate the rms differences from observations as 173, 183, and 252 m for CCSM4, OCN, and CCSM3, respectively. These indicate that while there are still significant differences from observations, MLDs in CCSM4 and OCN represent improvements over the CCSM3 MLDs. In particular, these improvements include shallower MLDs off Antarctica and reduced magnitudes of the dipole bias structure in the midlatitude Western Pacific in CCSM4 and OCN. Unfortunately, the shallow biases along the ACC path in CCSM3 get even shallower in the new CCSM4 and OCN simulations. In all cases, there are equally large and sometimes opposite biases of either sign in the high-latitude North Atlantic and GIN Seas.

h. Chlorofluorocarbon distributions

Chlorofluorocarbons (CFCs) have been entering the atmosphere since the 1930s, with concentrations leveling in the mid-1990s, following the Montreal Protocol. CFCs enter the ocean via air–sea gas exchange at the surface. They have a strong temperature-dependent solubility such that cold high-latitude waters take up far more CFC than warmer low-latitude waters. CFCs have been widely measured in the global ocean, mainly during the World Ocean Circulation Experiment (WOCE) program of the 1990s and more recently the CLIVAR cruises of the early twenty-first century. Here, we use an objectively mapped global CFC-11 *climatology* for 1994 from Global Ocean Data Analysis Project (GLODAP; Key et al. 2004) to assess model skill at reproducing global and column integrals of CFC-11 along with a select WOCE section to investigate regions of large model bias. For bias attribution purposes, we also consider CFC-11 partial pressure (pCFC-11) distributions, as pCFC-11 largely removes the effects of temperature biases in the

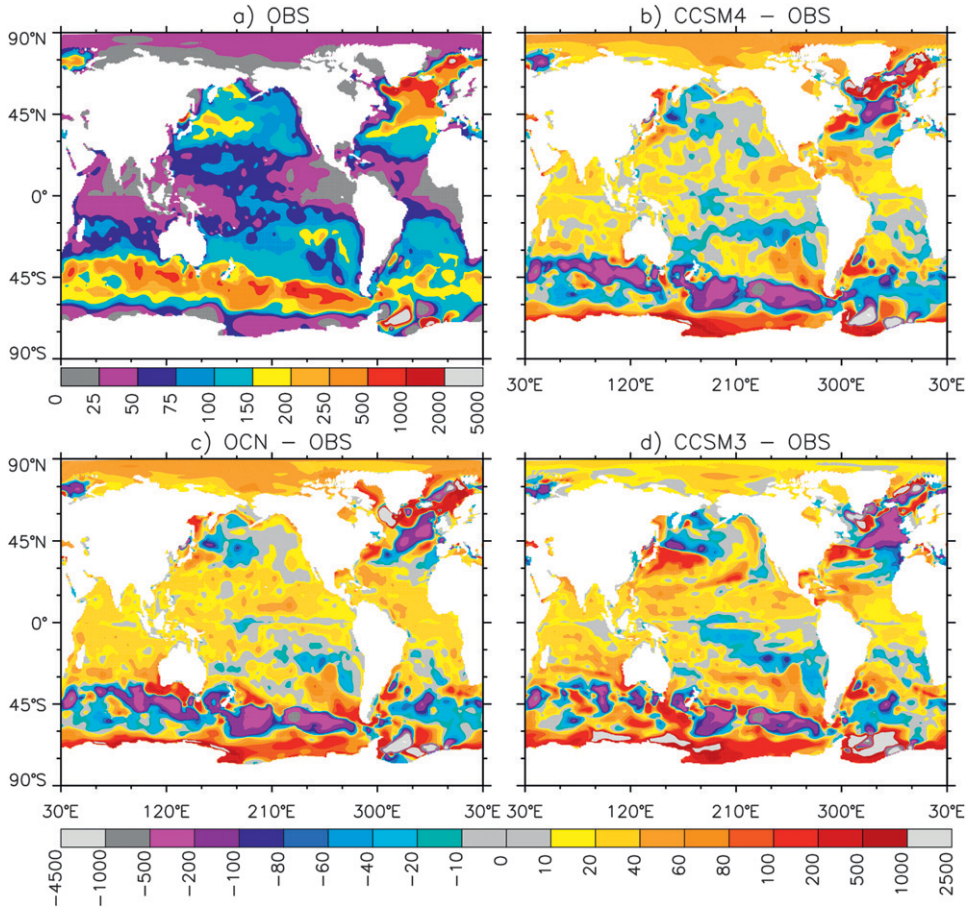

FIG. 19. Winter-mean mixed layer depth (m) from (a) observational estimate based on PHC2 data and model minus observations (OBS) differences for (b) CCSM4 – OBS, (c) OCN – OBS, and (d) CCSM3 – OBS. The winter means represent January, February, March and July, August, September averages in the Northern and Southern Hemispheres, respectively. The difference plots share the same color bar.

models, thus exposing impacts of circulation and ventilation changes.

Figure 20 presents the CFC-11 column inventories from CCSM4, CCSM3, and OCN in comparison with the GLODAP data, showing that the model simulations successfully reproduce the large scale features of the observed inventory. All simulations have their largest biases in the northern North Atlantic with CFC-11 inventories as high as 15 mol km^{-2}, thus representing positive biases of >3 mol km^{-2}. As revealed by the model minus observations difference distributions, CCSM4 shows significant reductions of the excessive CFC-11 uptake in the CCSM3 solutions in the Southern Ocean and South Pacific. The corresponding pCFC-11 distributions (not shown) indicate that this CCSM4 improvement in the Southern Ocean is due to both reduced ventilation—as also suggested by the shallower mixed layer depths (Fig. 19)—and generally smaller negative SST biases in CCSM4. While the former likely results from reductions in the wind stress strength and represents a model degradation, the latter represents a model improvement, producing diminished CFC-11 solubility. The negative bias region off Antarctica in the Atlantic Sector still persists in CCSM4. Elsewhere, in comparison with CCSM3, while there are some minor improvements in CCSM4 in the midlatitude North Pacific, the south Indian Ocean CFC-11 inventories are slightly worse in CCSM4. The Atlantic Ocean inventories are remarkably similar in both CCSM3 and CCSM4. Excluding the Arctic Ocean, GIN seas, and marginal seas, we calculate the global CFC-11 inventories as 4.6×10^8, 4.9×10^8, and 5.5×10^8 moles for 1994 for OCN, CCSM4, and CCSM3, respectively. The corresponding observational estimate is $5.4 \pm 0.8 \times 10^8$ moles. Although there is a 10% reduction in the global CFC-11 inventory in CCSM4 compared to CCSM3, the CCSM4 inventory remains within the range of observational estimates. The OCN inventory is barely within the GLODAP range, and both the column and global

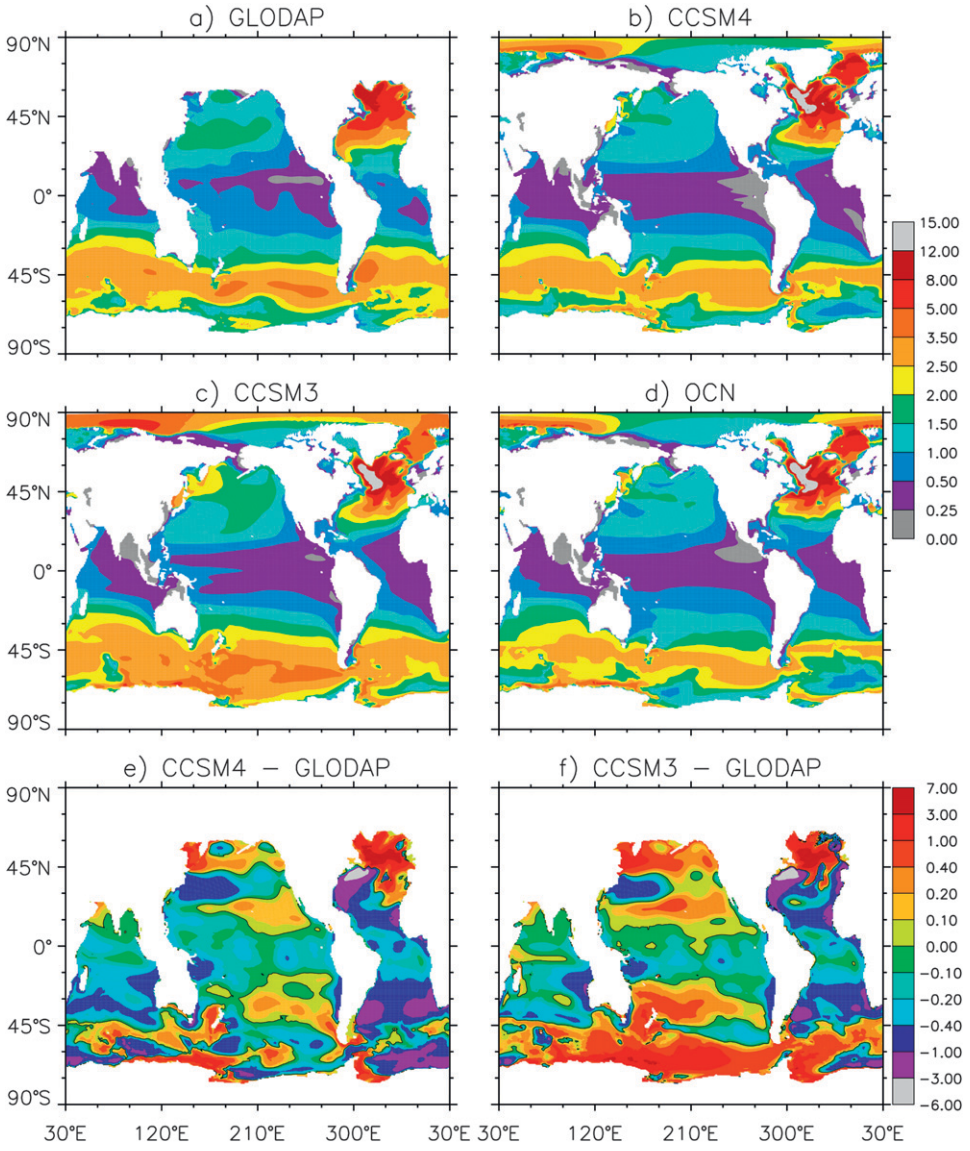

FIG. 20. CFC-11 column inventory (moles km^{-2}) from (a) GLODAP, (b) CCSM4, (c) CCSM3, and (d) OCN. The inventory differences for (e) CCSM4 – GLODAP and (f) CCSM3 – GLODAP are shown.

inventories are very similar to those of the ocean-only simulations with CCSM3 discussed in Danabasoglu et al. (2009).

To investigate the large positive CFC-11 biases in the model simulations in the high-latitude North Atlantic, we compare model solutions to observational data along the WOCE A24N section for 1997 in Fig. 21. The A24N is a diagonal section roughly between Scotland and Greenland just south of Iceland, and thus directly downstream of the DS and FBC overflow regions. The observations show CFC-11 concentrations of <3 pmol kg^{-1} below about 1000-m depth between 330° and 350°E. The lowest CFC-11 concentrations are found in the deepest regions of the Rockall Channel (near 350°E, southwest of the Wyville–Thomson Ridge) and of the Iceland Basin. Elevated levels of CFC-11 concentrations between 1000- and 2000-m depth near the western boundary of the section are due to the Labrador Seawater (LSW) flow into the Irminger Sea (see also Rhein et al. 2002). The CFC-11 maximum at the bottom between 325° and 330°E is the signature of the DS overflow water. We note that the observations suggest the FBC overflow water carries low levels of CFC-11 concentrations. The modeled concentrations are generally >3 pmol kg^{-1} west of 345°E for depths >1000 m. The intrusion of the low concentration tongue into the western half of the section seen in the

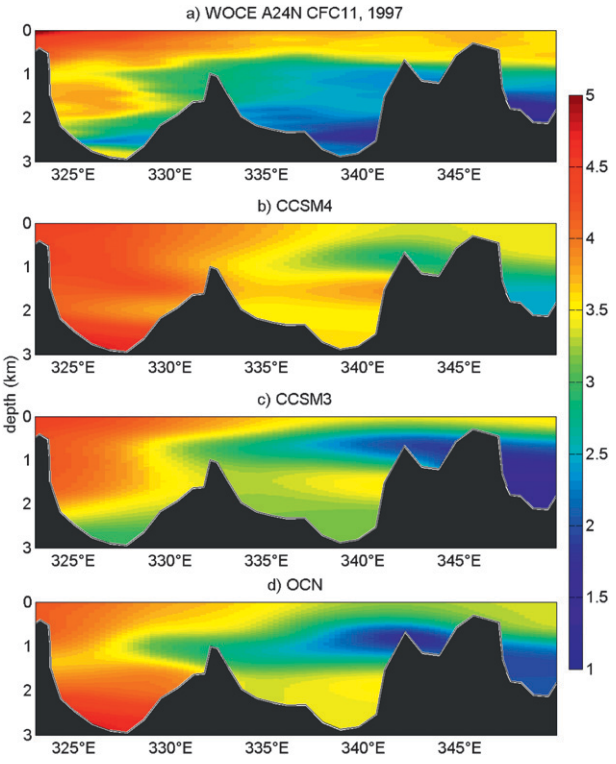

FIG. 21. CFC-11 concentration (pmol kg^{-1}) along the WOCE A24N section for 1997: (a) WOCE observational data, (b) CCSM4, (c) CCSM3, and (d) OCN.

WOCE data is captured well in OCN and to a lesser degree in CCSM3. The low CFC-11 concentrations in the Rockall Channel are present in all, but the agreement with the observations is better in CCSM3. In all model solutions, there is a maximum adjacent to topography at about 340°E in the Iceland Basin. This is due to the flow into this basin bringing high CFC-11 concentrations primarily from the northwestern North Atlantic. Slightly elevated CFC-11 levels at depth in the basin in CCSM4 represents the higher-than-observed levels of CFC-11 present in the FBC overflow water. In CCSM4 and OCN, high CFC-11 concentrations (>4.5 pmol kg^{-1}) clearly evident at depth in the Irminger Basin are due to the DS overflow waters, which are entirely absent in CCSM3. Above the DS overflow waters near the western boundary, both CCSM4 and OCN show LSW flow into the Irminger Basin, but it occurs at deeper levels in OCN than in CCSM4 and its CFC-11 signature is mixed with that of the DS overflow. The CFC-11 maximum between 1000- and 2000-m depth in CCSM3 results primarily from high CFC-11 concentrations carried by the rather wide East Greenland Current. Secondary contributions come from the flow bringing CFC-11 from the convection region slightly southeast of Cape Farewell (see Fig. 18b). The cold SST bias present in the DS source region in both CCSM4 and OCN is colder than in CCSM3 (see Fig. 6), resulting in increased CFC-11 solubility in the former cases. Indeed, a comparison of the surface CFC-11 concentrations between CCSM4 and CCSM3 reveals that the concentrations are larger by as much as 1.5–2 pmol kg^{-1} in CCSM4, particularly in the DS source region (not shown). Consequently, in CCSM4 and OCN the excessive CFC-11 uptake in the northern North Atlantic is likely due to cold SST biases in the DS region. In contrast, the excessive CFC-11 uptake in CCSM3 may be due to colder SSTs present in the Labrador Sea and high- to midlatitude North Atlantic (Fig. 6). The pCFC-11 column inventories (not shown) confirm that the model temperature biases are primarily responsible for the excessive CFC-11 uptake in the northern North Atlantic as model minus GLODAP pCFC-11 inventory differences show negative model biases in this region, suggesting low ventilation rates in both CCSM4 and CCSM3. However, the negative biases in CCSM4 are much reduced compared to CCSM3, likely due to the deep mixed layer biases in the high-latitude North Atlantic (see Fig. 19) in CCSM4.

4. Summary and conclusions

We have described the CCSM4 ocean component and documented its time-mean solutions from the 20C coupled simulations in comparison with available observations and those of CCSM3. The new ocean model differs significantly from its predecessor used in CCSM3; the base code has been updated to POP version 2 and many physical and numerical software developments have been implemented. The improvements to the physical processes include i) new parameterizations to represent previously missing physics such as gravity current overflows and abyssal tidal mixing and ii) modifications of existing parameterizations along with different prescriptions for their parameter choices to incorporate new information from recent observations as well as from eddy-permitting–resolving simulations. In addition, the number of vertical levels has been increased from 40 in CCSM3 to 60 in the present version, with most of this increase occurring in the upper ocean. The overarching motivation for these developments is to address coupled model biases through advances in model physics. Of course, there are no guarantees that better physics will lead to reduced biases as improvements can impact existing compensating biases and expose other new ones in coupled simulations. The individual impacts of these new developments and resulting improvements in ocean model solutions had been previously documented, using intermediate versions of both the ocean model and the coupled

system. The present work examines their cumulative impacts in the released CCSM4 version.

There are significant improvements in the ocean model solutions compared to those of CCSM3 that result from physics changes in the ocean model. These include an equatorial current structure, a sharper thermocline, and elimination of the cold bias of the equatorial cold tongue all in the Pacific Ocean; reduced SST and SSS biases along the North Atlantic Current path; deep convection site in the central Labrador Sea; much reduced potential temperature and salinity biases in the upper Pacific Ocean; and reduced ACC transport at Drake Passage (but still larger than observed). The reduced horizontal viscosities also lead to sea ice distributions that compare more favorably with observations in the northern North Atlantic, particularly in the Labrador Sea. Other improvements in the ocean model solutions include reduced SSS biases at low latitudes resulting from improved precipitation in these regions, significant reductions in the excessive CFC-11 uptake of CCSM3 in the Southern Ocean, and a global-mean SST that is more consistent with the present-day observations. The latter is due to the different spinup procedure used in CCSM4 than in CCSM3.

The ocean model solutions also show that CCSM4 still has many of the biases that were present in CCSM3. Some particular examples are warmer-than-observed SSTs originating in upwelling regions along the west coasts of North and South America and South Africa, colder-than-observed subthermocline waters in the equatorial Pacific, and excessive CFC-11 uptake in the northern North Atlantic. Despite the significant reductions in their surface magnitudes, upper-ocean potential temperature and salinity biases along the Gulf Stream and North Atlantic Current paths still exist with somewhat smaller magnitudes in CCSM4 than in CCSM3. Both atmospheric forcing and ocean model deficiencies contribute to these persistent biases. Some of these remaining biases, for example, the ones in the North Atlantic, expose circulation problems associated with dynamical shortcomings of noneddy-resolving ocean models such as the present one. As discussed in Bryan et al. (2007), eddy-resolving–permitting simulations show improved representations of the North Atlantic with realistic Gulf Stream separation and North Atlantic Current path and with water masses in good agreement with observations. While the use of globally eddy-resolving–permitting resolutions is not feasible for long climate simulations at present, regional mesh refinement needs to be explored.

A major concern continues to be the substantial heat content loss in the ocean component. Throughout the 1300-yr preindustrial control simulation, the ocean heat loss rate remains rather steady at about -0.15 W m^{-2}, corresponding to $\frac{2}{3}$ of the TOA heat loss of the coupled system. It is quite troubling that this trend does not get any smaller during the last 700 yr of integration and the global-mean potential temperature gets continuously colder. Thus, this seemingly small TOA heat flux imbalance leads to significant cooling trends in the ocean model at all depths with colder-than-observed deep Southern, Pacific, and Indian Ocean basins. It determines the abyssal ocean potential temperature biases in the subsequent 20C simulations as these are run only for 156 yr, too short to produce any significant changes from their initial conditions.

Despite a small global-mean trend, the ocean salt content gets redistributed, producing fresh and salty biases in the upper and deep oceans, respectively. A likely northern source for the deep salty bias is the Labrador Sea convection. The southern source appears to be the saltier-than-observed AABW. This is likely due to excessive sea ice formation in the coupled model with stronger winds. In the Southern, Pacific, and Indian abyssal basins, the cold and salty biases both act to produce waters that are denser than observed. In the Atlantic Ocean, although warm and salty biases are density compensating, salinity bias dominates producing higher-than-observed densities. In the deep North Atlantic, this has important adverse consequences—the parameterized overflow waters cannot penetrate much deeper and only minor improvements in the NADW penetration depth are realized in CCSM4 compared to that of CCSM3.

The ocean model will continue to evolve to further improve the model and its solutions and to address the remaining (or new) coupled model biases in collaboration with the broader oceanography community through U.S. CLIVAR CPTs and CCSM Ocean Model Working Group. Some work is already underway on internal wave driven mixing and the North Atlantic biases, the latter also considering the role of increased resolution. In addition, we believe that other important steps for the next version of the coupled model are to explore alternatives to further reduce the TOA heat flux imbalances and to investigate why the approach to equilibrium remains slow in the coupled system.

Acknowledgments. We thank all the scientists and software engineers who contributed to the development of the CCSM4. We particularly thank members of the CCSM Ocean Model Working Group. We thank two anonymous reviewers for their very constructive and useful comments. NCAR is sponsored by the National Science Foundation. The CCSM is also sponsored by the Department of Energy. SGY was supported by the NOAA Climate Program Office under Climate Variability and Predictability Program Grant NA09OAR4310163. Computing resources were provided by the Climate Simulation Laboratory at NCAR's Computational and

Information Systems Laboratory (CISL), sponsored by the National Science Foundation and other agencies. This research was enabled by CISL compute and storage resources. Bluefire, a 4064-processor IBM Power6 resource with a peak of 77 TeraFLOPS, provided more than 7.5 million computing hours, the GLADE high-speed disk resources provided 0.4 PetaBytes of dedicated disk, and CISL's 12-PB HPSS archive provided over 1 PetaByte of storage in support of this research project.

REFERENCES

Briegleb, B. P., G. Danabasoglu, and W. G. Large, 2010: An overflow parameterization for the ocean component of the Community Climate System Model. NCAR Tech. Note NCAR/TN-481+STR, 72 pp.

Bryan, F. O., G. Danabasoglu, P. R. Gent, and K. Lindsay, 2006: Changes in ocean ventilation during the 21st century in the CCSM3. *Ocean Modell.,* **15,** 141–156, doi:10.1016/j.ocemod.2006.01.002.

——, M. W. Hecht, and R. D. Smith, 2007: Resolution convergence and sensitivity studies with North Atlantic circulation models. Part I: The western boundary current system. *Ocean Modell.,* **16,** 141–159, doi:10.1016/j.ocemod.2006.08.005.

Collins, W. D., and Coauthors, 2006: The Community Climate System Model version 3 (CCSM3). *J. Climate,* **19,** 2122–2143.

Cunningham, S. A., S. G. Alderson, B. A. King, and M. A. Brandon, 2003: Transport and variability of the Antarctic Circumpolar Current in Drake Passage. *J. Geophys. Res.,* **108,** 8084, doi:10.1029/2001JC001147.

——, and Coauthors, 2007: Temporal variability of the Atlantic meridional overturning circulation at 26.5°N. *Science,* **317,** 935–938, doi:10.1126/science.1141304.

Dai, A., and K. E. Trenberth, 2002: Estimates of freshwater discharge from continents: Latitudinal and seasonal variations. *J. Hydrometeor.,* **3,** 660–687.

Danabasoglu, G., and J. Marshall, 2007: Effects of vertical variations of thickness diffusivity in an ocean general circulation model. *Ocean Modell.,* **18,** 122–141, doi:10.1016/j.ocemod.2007.03.006.

——, W. G. Large, J. J. Tribbia, P. R. Gent, B. P. Briegleb, and J. C. McWilliams, 2006: Diurnal coupling in the tropical oceans of CCSM3. *J. Climate,* **19,** 2347–2365.

——, R. Ferrari, and J. C. McWilliams, 2008: Sensitivity of an ocean general circulation model to a parameterization of near-surface eddy fluxes. *J. Climate,* **21,** 1192–1208.

——, S. Peacock, K. Lindsay, and D. Tsumune, 2009: Sensitivity of CFC-11 uptake to physical initial conditions and interannually varying surface forcing in a global ocean model. *Ocean Modell.,* **29,** 58–65, doi:10.1016/j.ocemod.2009.02.011.

——, W. G. Large, and B. P. Briegleb, 2010: Climate impacts of parameterized Nordic Sea overflows. *J. Geophys. Res.,* **115,** C11005, doi:10.1029/2010JC006243.

Dickson, R. R., and J. Brown, 1994: The production of North Atlantic Deep Water: Sources, rates, and pathways. *J. Geophys. Res.,* **99,** 12 319–12 341.

DiMarco, S. F., P. Chapman, W. D. Nowlin Jr., P. Hacker, K. Donohue, M. Luther, G. C. Johnson, and J. Toole, 2002: Volume transport and property distributions of the Mozambique Channel. *Deep-Sea Res. II,* **49,** 1481–1511.

Dye, S., B. Hansen, S. Osterhus, D. Quadfasel, and B. Rudels, 2007: The overflow of dense water across the Greenland-Scotland Ridge. *CLIVAR Exchanges,* Vol. 12, International CLIVAR Project Office, Southampton, United Kingdom, 20–22.

Ferrari, R., J. C. McWilliams, V. M. Canuto, and M. Dubovikov, 2008: Parameterization of eddy fluxes near oceanic boundaries. *J. Climate,* **21,** 2770–2789.

Ferreira, D., J. Marshall, and P. Heimbach, 2005: Estimating eddy stresses by fitting dynamics to observations using a residual-mean ocean circulation model and its adjoint. *J. Phys. Oceanogr.,* **35,** 1891–1910.

Foldvick, A., and Coauthors, 2004: Ice shelf water overflow and bottom water formation in the southern Weddell Sea. *J. Geophys. Res.,* **109,** C02015, doi:10.1029/2003JC002008.

Fox-Kemper, B., R. Ferrari, and R. Hallberg, 2008: Parameterization of mixed layer eddies. Part I: Theory and diagnosis. *J. Phys. Oceanogr.,* **38,** 1145–1165.

——, and Coauthors, 2011: Parameterization of mixed layer eddies. Part III: Implementation and impact in global ocean climate simulations. *Ocean Modell.,* **39,** 61–78, doi:10.1016/j.ocemod.2010.09.002.

Gent, P. R., and J. C. McWilliams, 1990: Isopycnal mixing in ocean circulation models. *J. Phys. Oceanogr.,* **20,** 150–155.

——, F. O. Bryan, G. Danabasoglu, K. Lindsay, D. Tsumune, M. W. Hecht, and S. C. Doney, 2006: Ocean chlorofluorocarbon and heat uptake during the twentieth century in the CCSM3. *J. Climate,* **19,** 2366–2381.

——, and Coauthors, 2011: The Community Climate System Model version 4. *J. Climate,* **24,** 4973–4991.

Girton, J. B., and T. B. Sanford, 2003: Descent and modification of the overflow plume in the Denmark Strait. *J. Phys. Oceanogr.,* **33,** 1351–1363.

Gordon, A. L., E. Zambianchi, A. Orsi, M. Visbeck, C. Giulivi, T. Whitworth, and G. Spezie, 2004: Energetic plumes over the western Ross Sea continental slope. *Geophys. Res. Lett.,* **31,** L21302, doi:10.1029/2004GL020785.

——, and Coauthors, 2010: The Indonesian throughflow during 2004-2006 as observed by the INSTANT program. *Dyn. Atmos. Oceans,* **50,** 115–128, doi:10.1016/j.dynatmoce.2009.12.002.

Griffies, S. M., 1998: The Gent–McWilliams skew flux. *J. Phys. Oceanogr.,* **28,** 831–841.

——, and Coauthors, 2009: Coordinated Ocean-Ice Reference Experiments (COREs). *Ocean Modell.,* **26,** 1–46, doi:10.1016/j.ocemod.2008.08.007.

Grodsky, S. A., J. A. Carton, S. Nigam, and Y. Okumura, 2012: Tropical Atlantic biases in CCSM4. *J. Climate,* in press.

Hamilton, P., J. Larsen, K. Leaman, T. Lee, and E. Waddell, 2005: Transports through the Straits of Florida. *J. Phys. Oceanogr.,* **35,** 308–322.

Hansen, D. V., and C. Paul, 1984: Genesis and effects of long waves in the equatorial Pacific. *J. Geophys. Res.,* **89,** 10 431–10 440.

Holland, M., D. A. Bailey, B. P. Briegleb, B. Light, and E. Hunke, 2012: Improved sea ice shortwave radiation physics in CCSM4: The impact of melt ponds and aerosols on Arctic Sea ice. *J. Climate,* **25,** 1413–1430.

Hurrell, J. W., J. J. Hack, D. Shea, J. M. Caron, and J. Rosinski, 2008: A new sea surface temperature and sea ice boundary dataset for the Community Atmosphere Model. *J. Climate,* **21,** 5145–5153.

Jayne, S. R., 2009: The impact of abyssal mixing parameterizations in an ocean general circulation model. *J. Phys. Oceanogr.,* **39,** 1756–1775.

Jochum, M., 2009: Impact of latitudinal variations in vertical diffusivity on climate simulations. *J. Geophys. Res.,* **114,** C01010, doi:10.1029/2008JC005030.

——, and J. Potemra, 2008: Sensitivity of tropical rainfall to Banda Sea diffusivity in the Community Climate System Model. *J. Climate,* **21,** 6445–6454.

——, R. Murtugudde, R. Ferrari, and P. Malanotte-Rizzoli, 2005: The impact of horizontal resolution on the equatorial mixed layer heat budget in ocean general circulation models. *J. Climate,* **18,** 841–851.

——, G. Danabasoglu, M. Holland, Y.-O. Kwon, and W. G. Large, 2008: Ocean viscosity and climate. *J. Geophys. Res.,* **113,** C06017, doi:10.1029/2007JC004515.

Johns, W. E., and Coauthors, 2011: Continuous, array-based estimates of Atlantic Ocean heat transport at 26.5°N. *J. Climate,* **24,** 2429–2449.

Johnson, G., B. Sloyan, W. Kessler, and K. McTaggart, 2002: Direct measurements of upper ocean currents and water properties across the tropical Pacific during the 1990s. *Prog. Oceanogr.,* **52,** 31–61.

Key, R. M., and Coauthors, 2004: A global ocean carbon climatology: Results from Global Data Analysis Project (GLODAP). *Global Biogeochem. Cycles,* **18,** GB4031, doi:10.1029/2004GB002247.

Large, W. G., and G. Danabasoglu, 2006: Attribution and impacts of upper-ocean biases in CCSM3. *J. Climate,* **19,** 2325–2346.

——, and S. G. Yeager, 2009: The global climatology of an interannually varying air-sea flux data set. *Climate Dyn.,* **33,** 341–364, doi:10.1007/s00382-008-0441-3.

——, J. C. McWilliams, and S. C. Doney, 1994: Oceanic vertical mixing: A review and a model with a nonlocal boundary layer parameterization. *Rev. Geophys.,* **32,** 363–403.

——, G. Danabasoglu, J. C. McWilliams, P. R. Gent, and F. O. Bryan, 2001: Equatorial circulation in a global ocean climate model with anisotropic horizontal viscosity. *J. Phys. Oceanogr.,* **31,** 518–536.

Lavender, K. L., R. E. Davis, and W. B. Owens, 2002: Observations of open-ocean deep convection in the Labrador Sea from subsurface floats. *J. Phys. Oceanogr.,* **32,** 511–526.

Legg, S., and Coauthors, 2009: Improving oceanic overflow representation in climate models: The gravity current entrainment climate process team. *Bull. Amer. Meteor. Soc.,* **90,** 657–670.

Levitus, S., T. Boyer, M. Concright, D. Johnson, T. O'Brien, J. Antonov, C. Stephens, and R. Garfield, 1998: *Introduction*. Vol. I, *World Ocean Database 1998,* NOAA Atlas NESDIS 18, 346 pp.

Macrander, A., U. Send, H. Valdimarsson, S. Jonsson, and R. H. Kase, 2005: Interannual changes in the overflow from the Nordic Seas into the Atlantic Ocean through Denmark Strait. *Geopyhs. Res. Lett.,* **32,** L06606, doi:10.1029/2004GL021463.

——, R. H. Kase, U. Send, H. Valdimarsson, and S. Jonsson, 2007: Spatial and temporal structure of the Denmark Strait overflow revealed by acoustic observations. *Ocean Dyn.,* **57,** 75–89.

Mauritzen, C., J. Price, T. Sanford, and D. Torres, 2005: Circulation and mixing in the Faroese Channels. *Deep-Sea Res. I,* **52,** 883–913.

McCreary, J. P. J., 1981: A linear stratified ocean model of the equatorial undercurrent. *Philos. Trans. Roy. Soc. London,* **298,** 603–645.

McPhaden, M. J., and Coauthors, 1998: The tropical ocean-global atmosphere observing system: A decade of progress. *J. Geophys. Res.,* **103,** 14 169–14 240.

Munk, W. H., 1950: On the wind-driven ocean circulation. *J. Meteor.,* **7,** 79–93.

National Geophysical Data Center, 2006: ETOPO2v2: 2-minute gridded global relief data. U.S. Department of Commerce, National Oceanic and Atmospheric Administration, National Geophysical Data Center. [Available online at http://www.ngdc.noaa.gov/mgg/fliers/06mgg01.html.]

Neale, R. B., J. H. Richter, and M. Jochum, 2008: The impact of convection on ENSO: From a delayed oscillator to a series of events. *J. Climate,* **21,** 5904–5924.

Oleson, K. W., and Coauthors, 2010: Technical description of version 4.0 of the Community Land Model (CLM). NCAR Tech. Note NCAR/TN-478+STR, 257 pp.

Orsi, A. H., G. C. Johnson, and J. L. Bullister, 1999: Circulation, mixing, and production of Antarctic Bottom Water. *Prog. Oceanogr.,* **43,** 55–109.

——, W. M. Smethie, and J. L. Bullister, 2002: On the total input of Antarctic waters to the deep ocean: A preliminary estimate from chlorofluorocarbon measurements. *J. Geophys. Res.,* **107,** 3122, doi:10.1029/2001JC000976.

Price, J., and J. Yang, 1998: Marginal sea overflows for climate simulations. *Ocean Modeling and Parameterization,* E. P. Chassignet and J. Verron, Eds., Kluwer Academic, 155–170.

Rhein, M., and Coauthors, 2002: Labrador Sea water: Pathways, CFC inventory, and formation rates. *J. Phys. Oceanogr.,* **32,** 648–665.

Roach, A., K. Aagaard, C. Pease, S. A. Salo, T. Weingartner, V. Pavlov, and M. Kulakov, 1995: Direct measurements of transport and water properties through the Bering Strait. *J. Geophys. Res.,* **100,** 18 443–18 458.

Shields, C., D. Bailey, G. Danabasoglu, M. Jochum, and R. Neale, 2012: Low-resolution CCSM4. *J. Climate,* in press.

Smith, R. D., and J. C. McWilliams, 2003: Anisotropic horizontal viscosity for ocean models. *Ocean Modell.,* **5,** 129–156.

——, and Coauthors, 2010: The Parallel Ocean Program (POP) reference manual, ocean component of the Community Climate System Model (CCSM). Los Alamos National Laboratory Tech. Rep. LAUR-10-01853, 141 pp. [Available online at http://www.cesm.ucar.edu/models/cesm1.0/pop2/doc/sci/POPRefManual.pdf.]

Steele, M., R. Morley, and W. Ermold, 2001: PHC: A global ocean hydrography with a high quality Arctic Ocean. *J. Climate,* **14,** 2079–2087.

St. Laurent, L. C., H. L. Simmons, and S. R. Jayne, 2002: Estimates of tidally driven enhanced mixing in the deep ocean. *Geophys. Res. Lett.,* **29,** 2106, doi:10.1029/2002GL015633.

Sverdrup, H. U., 1947: Wind driven currents in a baroclinic ocean with application to the equatorial currents in the eastern Pacific. *Proc. Natl. Acad. Sci. USA,* **33,** 318–326.

Toggweiler, J. R., K. Dixon, and W. S. Broecker, 1991: The Peru upwelling and the ventilation of the South-Pacific thermocline. *J. Geophys. Res.,* **96,** 20 467–20 497.

Weijer, W., and Coauthors, 2012: The Southern Ocean and its climate in CCSM4. *J. Climate,* in press.

Wu, W., G. Danabasoglu, and W. G. Large, 2007: On the effects of parameterized Mediterranean overflow on North Atlantic ocean circulation and climate. *Ocean Modell.,* **19,** 31–52, doi:10.1016/j.ocemod.2007.06.003.

Yeager, S. G., and M. Jochum, 2009: The connection between Labrador Sea buoyancy loss, deep western boundary current strength, and Gulf Stream path in an ocean circulation model. *Ocean Modell.,* **30,** 207–224, doi:10.1016/j.ocemod.2009.06.014.

——, and G. Danabasoglu, 2012: Sensitivity of Atlantic meridional overturning circulation variability to parameterized Nordic Sea overflows in CCSM4. *J. Climate,* in press.